



UNIVERSITÀ DI PARMA

ARCHIVIO DELLA RICERCA

University of Parma Research Repository

Inhalation of peptide-loaded nanoparticles improves heart failure

This is the peer reviewed version of the following article:

Original

Inhalation of peptide-loaded nanoparticles improves heart failure / Miragoli, Michele; Ceriotti, Paola; Iafisco, Michele; Vacchiano, Marco; Salvarani, Nicol  ; Alogna, Alessio; Carullo, Pierluigi; Ramirez-Rodr  guez, Gloria Bel  n; Patr  cio, Tatiana; DEGLI ESPOSTI, Lorenzo; Rossi, Francesca; Ravanetti, Francesca; Pinelli, Silvana; Alinovi, Rossella; Erreni, Marco; Rossi, Stefano; Condorelli, Gianluigi; Post, Heiner; Tampieri, Anna; Catalucci, Daniele. - In: SCIENCE TRANSLATIONAL MEDICINE. - ISSN 1946-6234. - 10:424(2018), p. ean6205. [10.1126/scitranslmed.aan6205]

Availability:

This version is available at: 11381/2837511 since: 2021-10-08T10:58:38Z

Publisher:

American Association for the Advancement of Science

Published

DOI:10.1126/scitranslmed.aan6205

Terms of use:

Anyone can freely access the full text of works made available as "Open Access". Works made available

Publisher copyright

note finali coverpage

(Article begins on next page)



Inhalation of peptide-loaded nanoparticles improves heart failure

Michele Miragoli,^{1,2,3,7,†*} Paola Ceriotti,^{1,3, †} Michele Iafisco,⁴ Marco Vacchiano,¹ Nicolò Salvarani,^{1,3} Alessio Alogna,^{5,6} Pierluigi Carullo,^{1,3} Gloria Belén Ramirez-Rodríguez,⁴ Tatiana Patrício,⁴ Lorenzo Degli Esposti,⁴ Francesca Rossi,⁷ Francesca Ravanetti,⁸ Silvana Pinelli,² Rossella Alinovi,² Marco Erreni,^{1,9} Stefano Rossi,² Gianluigi Condorelli,^{1,3,9} Heiner Post,⁵ Anna Tampieri,⁴ & Daniele Catalucci,^{1,3,*}

¹Humanitas Clinical and Research Center, Rozzano (Milan), 20089 Italy.

²Department of Medicine and Surgery, University of Parma, Parma, 43126 Italy.

³Institute of Genetics and Biomedical Research, Milan Unit, National Research Council, Milan 20138 Italy.

⁴Institute of Science and Technology for Ceramics, National Research Council, Faenza (Ravenna), 48018 Italy.

⁵Department of Internal Medicine and Cardiology, Campus Virchow Klinikum, Charité University Medicine Berlin, Berlin, 13353 Germany.

⁶Berlin Institute of Health (BIH), Berlin, 10117 Germany.

⁷Institute of Materials for Electronics and Magnetism, National Research Council, Parma, 43126, Italy

⁸Department of Veterinary Science, University of Parma, Parma, 43126, Italy

⁹Humanitas University, Rozzano (Milan), 20089 Italy.

* These authors equally contributed to the work.

† Correspondence to: Michele.miragoli@humanitasresearch.it and daniele.catalucci@cnr.it

Peptides are recognized for being highly selective and efficacious for the treatment of cardiovascular as well as other diseases but their administration via a non invasive procedure is currently not possible, thus representing scientific and technological challenges. Here we demonstrate that inhalation of small sized (<50nm) biocompatible and biodegradable calcium phosphate nanoparticles (CaPs) allows for rapid translocation of CaPs from the pulmonary tree to the blood stream and thus to the myocardium where their cargo is quickly released. In particular, treatment of a rodent model of diabetic cardiomyopathy through inhalation of CaPs loaded with a therapeutic mimetic peptide (MP) that we previously demonstrated to improve myocardial contraction resulted in restoration of cardiac function. When translated to large animals, tangible evidence that inhalation of a peptide-loaded CaP-formulation is a safe and valid method of cardio-targeted administration was provided. Altogether, these results demonstrate that

inhalation of biocompatible tailored peptide nanocarriers represents a pioneering approach for the pharmacological treatment of heart failure.

One Sentence Summary: Inhalation delivers drug-loaded nanoparticles to the heart.

INTRODUCTION

The application of nanotechnology to medicine (the so-called nanomedicine) is at the forefront of innovation for modern health care and represents at present the most promising approach for efficient delivery of therapeutics (1-3). In line with this, a collection of first-generation nano-products for clinical use have recently been approved by the Food and Drug Administration, and other liposomal and polymer drug conjugate nanosystems are under clinical and preclinical development (4-7). However, despite remarkable advances in the use of nanoparticles in the cancer field, very few preclinical tests have been reported for nanomedicine applied to the treatment of cardiovascular diseases (CVDs) (8-10) that, claiming 17.5 million lives a year and accounting for an estimated 31% of all deaths globally, stand as the leading cause of death worldwide (11). The identification of innovative therapeutic nanoformulations, alternative administrations routes, or a combination of both may help to overcome the limitations associated with current pharmacological treatments, leading to more specific and efficient therapies.

Drug administration for the treatment of myocardial disease currently includes either oral or needle-based routes (12). However, enteral resorption is unreliable during acute or chronic gastrointestinal congestion, while injection, either intravenously, subcutaneously, or intramuscular, is associated with patient discomfort and malcompliance, rendering these administrations suboptimal for chronic treatment. Moreover, home or ambulatory care is frequently required for injection procedures. To the best of our knowledge, no study has addressed the possibility of using nanoparticles that can treat cardiac conditions when inhaled. In fact, although inhalation delivery is a common procedure for the treatment of respiratory problems, no pharmacological therapies are, as far as we know, currently adopting any inhalation approach for the delivery of therapeutics such as peptides via nanoparticles to the heart for

treatment. Furthermore, despite of an increasing interest in peptide therapeutics in pharmaceutical research and development, no effective and non-invasive peptide-based treatment of cardiac dysfunction has been successfully developed so far, leaving the parental route (*i.e.* injection) the only currently available option (13, 14).

Here we show that an approach of inhalation therapy is effective for delivering nanoparticle-based therapeutic peptide to the diseased heart.

RESULTS

We have recently developed biocompatible and bioresorbable negatively charged CaPs that via a biomineralization-inspired strategy are produced with a size ranging from 20 to 50 nm and are able to deliver bioactive molecules to cardiac cells (15). Without promoting toxicity or interfering with any functional properties of cardiomyocytes, CaPs were shown *in vitro* to safely and successfully cross the cardiomyocyte cellular membrane and release bioactive molecules (*i.e.* microRNAs) inside the cell (15). We thus sought to assess whether cardiac targeting of CaPs could be applied for the delivery of therapeutic peptides via the respiratory tree through inhalation (Fig. 1a). The rationale for the use of this unconventional administration route for targeting of the heart is based on the concepts that *i)* during respiration, the oxygenated blood moves from the pulmonary circulation first to the heart via the pulmonary vein, and *ii)* combustion-derived nanoparticles and ultra-fine particulates inhaled through polluted air was recently shown by us (16) and others (17) to be present in the heart and causally associated with cardiac arrhythmia and dysfunction, suggesting that inhaled nanoparticles get deposited in the heart. Furthermore, CaPs can protect peptides from immediate enzymatic degradation and thanks to their negative surface charge our nanoparticles provide cellular permeability via membrane

internalizing properties (15, 18). Thus, we predicted that inhaled small-sized CaPs would be able to cross the alveolar-capillary barrier in the lung and rapidly translocate to the myocardium for safe intracellular release of therapeutic peptides.

To assess heart targeting following nanoparticle administration, we first generated near-infrared fluorophore-loaded CaPs (CaP-Cy7) (fig. S1,2, table S1, and supplementary results) and delivered to healthy mice. Thereafter, fluorescence measurements were performed to compare distinct administration routes, which, in addition to conventional ways (*i.e.* oral, intraperitoneal, and intravenous), included nebulization of CaP-Cy7 via the respiratory route. Whereas enteral administration (*i.e.* gavage) did not result in statistically significant targeting to the heart at 40 min post administration, parenteral administration (*i.e.* intraperitoneal, intravenous, and inhalation) resulted in a rapid delivery of CaP-Cy7 to the myocardium with inhalation being the most efficient delivery method (Fig. 1b, c and fig. S3a-d). Notably, the time course of CaP-Cy7 myocardial accumulation was paralleled by a gradual reduction in signals from the lungs as a function of time, suggesting a continuous passage of nanoparticles across the pulmonary barrier (Fig. 1c and fig. S3d). Similar results were obtained via an optical *in vivo* imaging approach, which allowed us to monitor the behavior of inhaled CaP-Cy7 and their gradual accumulation in the mediastinum, the thoracic cavity containing the heart, esophagus, and trachea (Fig. 1d and fig. S3b). A delayed clearance of inhaled CaP-Cy7 was observed compared to Cy7 alone (Fig. 1d and fig. S3e), which was supported by 3D Fluorescence Molecular Tomography (FMT) imaging of the cardio-pulmonary area from mice analyzed 60 min after inhalation, revealing marked localization of CaP-Cy7 in the myocardium compared to Cy7 alone (Fig. 1e and video S1, S2). Effective delivery of CaP-Cy7 to the myocardium was further confirmed by fluorescence analyses on explanted hearts (Fig. 1f), while no specific cardiac targeting was found of Cy7

alone, which following rapid and broad diffusion in the lungs and the rest of the body rapidly accumulated in the bladder (Fig. 1d-f). In addition, no CaP-Cy7s were found to cross the blood-brain barrier (Fig. 1d, fig. S3c and data not shown). Targeting of CaP to the myocardium was also confirmed by transmission electron microscopy (fig. S3f,g). Notably, and in contrast to the toxic outcome associated with inhalation of nanoparticulates from polluted air and other inorganic nanoparticles such as TiO₂, SiO₂, and Co₃O₄ nanoparticles (19-22), pulmonary CaP administration (via single or multiple once-a-day administration protocols) did not affect cardiac function as measured by echocardiography (fig. S4 and table S2). In addition, no alterations in cardiac excitability and refractoriness were detected as shown by the absence of arrhythmogenic events as evaluated by *in vivo* epicardial multiple lead recordings (table S3). Furthermore, no toxicological (table S4) or immunological effects (no detectable changes in RNA levels of CD11, IL-1, TNF, IL-6, IL-4, and IL-5) were observed. In agreement with our recent work (15), the latter evidence supports the concept that biomimetic CaPs, closely resembling the inorganic phase of bone and teeth (23), are recognized by the body as endogenous material, thus being completely biocompatible and well tolerated *in vivo*.

Based on our demonstration that CaP inhalation allows nanoparticles to cross the pulmonary barrier and reach the heart, our next objective was to explore the use of peptide-loaded CaPs for cardiac treatment *in vivo*. We recently demonstrated the therapeutic effect of a cell-penetrating mimetic peptide (R7W-MP) that by targeting a cytosolic subunit of the L-type calcium channel (LTCC) on pathological heart conditions associated with alterations of LTCC levels and function (*i.e.* diabetic cardiomyopathy) improves cardiac contractility via restoration of LTCC density at the plasma membrane (24). Thus, to test the therapeutic use of the CaP for peptide delivery for the treatment of a cardiac condition, we treated a mouse model of

streptozotocin (STZ)-induced diabetic cardiomyopathy via inhalation of CaP loaded with R7W-free mimetic peptide (CaP-MP), preserving the physicochemical features (fig. S1, S2) of unloaded CaPs reported in our recent study (24). Due to the absence of the cell-internalizing R7W sequence on the MP, its efficiency in rescuing cardiac contractility would require the CaP to mediate its crossing of the pulmonary barrier and subsequent myocardial cell internalization. Supporting an ability of CaP to mediate cardiomyocyte internalization, stimulated emission depletion (STED) microscopy of isolated adult cardiomyocytes from mice treated with MP-Rhodamine-loaded CaPs showed effective targeting of the MP to cardiomyocytes, accounting for 124 ± 52 fluorescent signals per single cell (Fig. 2, video S3, and fig. S5f). Consistently, an inhalation approach of diabetic mice (Fig. 3a and fig. S5a) with CaP-MPs led to a complete recovery of cardiac function as shown by echocardiographic assessment of left ventricular function (Fig. 3b and table S5). Accordingly, improvement of molecular and cellular defects associated with diabetic cardiomyopathy was achieved as a result of the direct targeting of MP to LTCC (24), including restoration of LTCC protein levels (Fig. 3c and fig.S5c) as well as recovery of LTCC currents (Fig. 3d, and fig. S5d) and LTCC-related contractile (Fig. 3e) properties as determined in isolated cardiomyocytes from CaP-MP treated mice. In contrast, as expected, no therapeutic effects were obtained when hemagglutinin peptide (HA, scramble peptide)-loaded CaPs (CaP-HA) or unloaded (free) MP were administered (Fig. 3b-e, fig. S5d and table S5). Altogether, these data provide evidence that inhalation of MP-loaded CaPs is an effective approach for delivery of therapeutic peptides to the heart and demonstrate the benefit of CaP-MP inhalation in recovering LTCC-associated cardiac dysfunctions.

Finally, to advance towards clinical research in humans and generate the first proof of concept in large animals, safety and feasibility of cardiac targeting via our nanoparticle-based

inhalation approach was assessed by nebulization of CaP-HA in anaesthetized healthy landrace pigs (Fig. 4a). Similar to our results in mice, no changes in heart rate, mean arterial blood pressure, cardiac output (9.8 ± 0.8 vs 9.9 ± 0.8 l/min), as well as systemic and pulmonary vascular resistance were observed up to 5 hours from a single inhalation of CaP-HA (Fig. 4b,c). Left ventricular (LV) ejection fraction, as well as LV systolic and diastolic function as assessed by pressure derived parameters, such as the maximum rate of LV pressure increase and decrease (dP/dt max and dP/dt min), or via extensive pressure-volume analysis (end-diastolic and end-systolic pressure-volume relationships, Fig.4c) did not change. Furthermore, in the surface ECG no arrhythmias were detected, while PQ and QT intervals, as well as QRS duration did not change. Finally, respiratory function (end-tidal carbon dioxide partial pressure between 35 and 40 mmHg, and arterial oxygen saturation between 97 and 100% at a constant respiratory minute volume) was not affected by the inhalation of CaP-HA. In a separate series of pigs, myocardial biopsies from the left ventricular wall were taken at baseline and sequentially after treatment. At 300 min post inhalation, HA levels were significantly increased, providing evidence for effective delivery of CaP-HA to the myocardium (Fig. 4d). These data were supported by Western blot (Fig. 5e) and confocal microscopy (Fig. 5f) of cardiac tissue analyses. Altogether, these data confirm the efficiency and safety of our approach for the intra-myocardial delivery of compounds in large animal.

DISCUSSION

Here, we provide the proof-of-concept for a new avenue of innovative and unconventional nanotechnological approach for cardiac delivery of peptides for the treatment of pathological heart conditions. Inhalation per se has long been established for the treatment of pulmonary

diseases (25, 26), but its use for targeting of the heart and management of cardiac failing conditions has not previously been explored. We show that an inhalation therapy based on our biocompatible CaP nanocarriers allows for a safe targeting and treatment of the heart. In addition, we showed that nanoparticle accumulation in the heart is higher and faster when CaPs are inhaled compared to other delivery routes such as gavage, IP or IV. This lead to the conclusion that inhalation-facilitated cardiac drug delivery using nanomaterials potentially requires lower amounts of therapeutic compound, minimizing side effects compared to systemic delivery due to reduced first-pass metabolism. Moreover, inhalation is patient-friendly (easily administered), free from any physical and emotional burden associated with injection and/or any other minimally though invasive procedures, and facilitates patient compliance, convenience, and home-based chronic treatment. No such approach is currently available for targeting of the heart and may open up new avenues of investigation and potential uses of nanomaterials for the treatment of CVD with peptides. A broader use for other drug/diagnostic compounds with different release kinetics (therapeutic polypharmacy) or even different tissue targeting can be envisaged.

References

1. M. Giardiello, N. J. Liptrott, T. O. McDonald, D. Moss, M. Siccardi, P. Martin, D. Smith, R. Gurjar, S. P. Rannard, A. Owen, Accelerated oral nanomedicine discovery from miniaturized screening to clinical production exemplified by paediatric HIV nanotherapies. *Nature communications* 7, 13184 (2016).
2. B. Y. Kim, J. T. Rutka, W. C. Chan, Nanomedicine. *The New England journal of medicine* 363, 2434-2443 (2010).

3. M. E. Davis, J. E. Zuckerman, C. H. Choi, D. Seligson, A. Tolcher, C. A. Alabi, Y. Yen, J. D. Heidel, A. Ribas, Evidence of RNAi in humans from systemically administered siRNA via targeted nanoparticles. *Nature* 464, 1067-1070 (2010).
4. V. Weissig, T. K. Pettinger, N. Murdock, Nanopharmaceuticals (part 1): products on the market. *International journal of nanomedicine* 9, 4357-4373 (2014).
5. R. Kuai, L. J. Ochyl, K. S. Bahjat, A. Schwendeman, J. J. Moon, Designer vaccine nanodiscs for personalized cancer immunotherapy. *Nat Mater*, (2016).
6. Y. Zhao, F. Fay, S. Hak, J. Manuel Perez-Aguilar, B. L. Sanchez-Gaytan, B. Goode, R. Duivenvoorden, C. de Lange Davies, A. Bjorkoy, H. Weinstein, Z. A. Fayad, C. Perez-Medina, W. J. Mulder, Augmenting drug-carrier compatibility improves tumour nanotherapy efficacy. *Nature communications* 7, 11221 (2016).
7. E. Blanco, H. Shen, M. Ferrari, Principles of nanoparticle design for overcoming biological barriers to drug delivery. *Nat Biotechnol* 33, 941-951 (2015).
8. Y. T. Ho, B. Poinard, J. C. Kah, Nanoparticle drug delivery systems and their use in cardiac tissue therapy. *Nanomedicine* 11, 693-714 (2016).
9. C. W. Evans, K. S. Iyer, L. C. Hool, The potential for nanotechnology to improve delivery of therapy to the acute ischemic heart. *Nanomedicine* 11, 817-832 (2016).
10. S. S. Behera, K. Pramanik, M. K. Nayak, Recent Advancement in the Treatment of Cardiovascular Diseases: Conventional Therapy to Nanotechnology. *Current pharmaceutical design* 21, 4479-4497 (2015).
11. S. Mendis, S. Davis, B. Norrving, Organizational update: the world health organization global status report on noncommunicable diseases 2014; one more landmark step in the

- combat against stroke and vascular disease. *Stroke; a journal of cerebral circulation* 46, e121-122 (2015).
12. S. Suarez, A. Almutairi, K. L. Christman, Micro- and Nanoparticles for Treating Cardiovascular Disease. *Biomaterials science* 3, 564-580 (2015).
 13. K. Fosgerau, T. Hoffmann, Peptide therapeutics: current status and future directions. *Drug Discov Today* 20, 122-128 (2015).
 14. T. Uhlig, T. Kyprianou, F. G. Martinelli, C. A. Oppici, D. Heiligers, D. Hills, X. R. Calvo, P. Verhaert, The emergence of peptides in the pharmaceutical business: From exploration to exploitation. *EuPA Open Proteomics* 4, 58-69 (2014).
 15. V. Di Mauro, M. Iafisco, N. Salvarani, M. Vacchiano, P. Carullo, G. B. Ramirez-Rodriguez, T. Patricio, A. Tampieri, M. Miragoli, D. Catalucci, Bioinspired negatively charged calcium phosphate nanocarriers for cardiac delivery of MicroRNAs. *Nanomedicine* 11, 891-906 (2016).
 16. M. Savi, S. Rossi, L. Bocchi, L. Gennaccaro, F. Cacciani, A. Perotti, D. Amidani, R. Alinovi, M. Goldoni, I. Aliatis, P. P. Lottici, D. Bersani, M. Campanini, S. Pinelli, M. Petyx, C. Frati, A. Gervasi, K. Urbanek, F. Quaini, A. Buschini, D. Stilli, C. Rivetti, E. Macchi, A. Mutti, M. Miragoli, M. Zaniboni, Titanium dioxide nanoparticles promote arrhythmias via a direct interaction with rat cardiac tissue. *Particle and fibre toxicology* 11, 63 (2014).
 17. N. L. Mills, K. Donaldson, P. W. Hadoke, N. A. Boon, W. MacNee, F. R. Cassee, T. Sandstrom, A. Blomberg, D. E. Newby, Adverse cardiovascular effects of air pollution. *Nat Clin Pract Cardiovasc Med* 6, 36-44 (2009).

18. M. Miragoli, P. Novak, P. Ruenraroengsak, A. I. Shevchuk, Y. E. Korchev, M. J. Lab, T. D. Tetley, J. Gorelik, Functional interaction between charged nanoparticles and cardiac tissue: a new paradigm for cardiac arrhythmia? *Nanomedicine* 8, 725-737 (2013).
19. S. Bakand, A. Hayes, F. Dechsakulthorn, Nanoparticles: a review of particle toxicology following inhalation exposure. *Inhal Toxicol* 24, 125-135 (2012).
20. W. H. De Jong, P. J. Borm, Drug delivery and nanoparticles: applications and hazards. *International journal of nanomedicine* 3, 133-149 (2008).
21. J. R. Roberts, W. McKinney, H. Kan, K. Krajnak, D. G. Frazer, T. A. Thomas, S. Waugh, A. Kenyon, R. I. MacCuspie, V. A. Hackley, V. Castranova, Pulmonary and cardiovascular responses of rats to inhalation of silver nanoparticles. *J Toxicol Environ Health A* 76, 651-668 (2013).
22. L. Petrick, M. Rosenblat, N. Paland, M. Aviram, Silicon dioxide nanoparticles increase macrophage atherogenicity: Stimulation of cellular cytotoxicity, oxidative stress, and triglycerides accumulation. *Environ Toxicol* 31, 713-723 (2016).
23. K. Lin, C. Wu, J. Chang, Advances in synthesis of calcium phosphate crystals with controlled size and shape. *Acta Biomater* 10, 4071-4102 (2014).
24. F. Rusconi, P. Ceriotti, M. Miragoli, P. Carullo, N. Salvarani, M. Rocchetti, E. Di Pasquale, S. Rossi, M. Tessari, S. Caprari, M. Cazade, P. Kunderfranco, J. Chemin, M. L. Bang, F. Polticelli, A. Zaza, G. Faggian, G. Condorelli, D. Catalucci, Peptidomimetic Targeting of Cavbeta2 Overcomes Dysregulation of the L-Type Calcium Channel Density and Recovers Cardiac Function. *Circulation* 134, 534-546 (2016).

25. J. S. Patton, C. S. Fishburn, J. G. Weers, The lungs as a portal of entry for systemic drug delivery. *Proc Am Thorac Soc* 1, 338-344 (2004).
26. M. Irngartinger, V. Camuglia, M. Damm, J. Goede, H. W. Frijlink, Pulmonary delivery of therapeutic peptides via dry powder inhalation: effects of micronisation and manufacturing. *European journal of pharmaceutics and biopharmaceutics: official journal of Arbeitsgemeinschaft fur Pharmazeutische Verfahrenstechnik e.V* 58, 7-14 (2004).

Acknowledgments: We acknowledge funding from the MIUR flagship Nanomax, 2013-2017 to D.C., M.M., A.T., H2020-NMBP-2016 720834 CUPIDO (www.cupidoproject.eu) to D.C., M.M., M.I., H.P. and in part the Italian Ministry of Health GR-2011-02352546 to D.C.

Marie-Louie Bang for critically reading the manuscript.

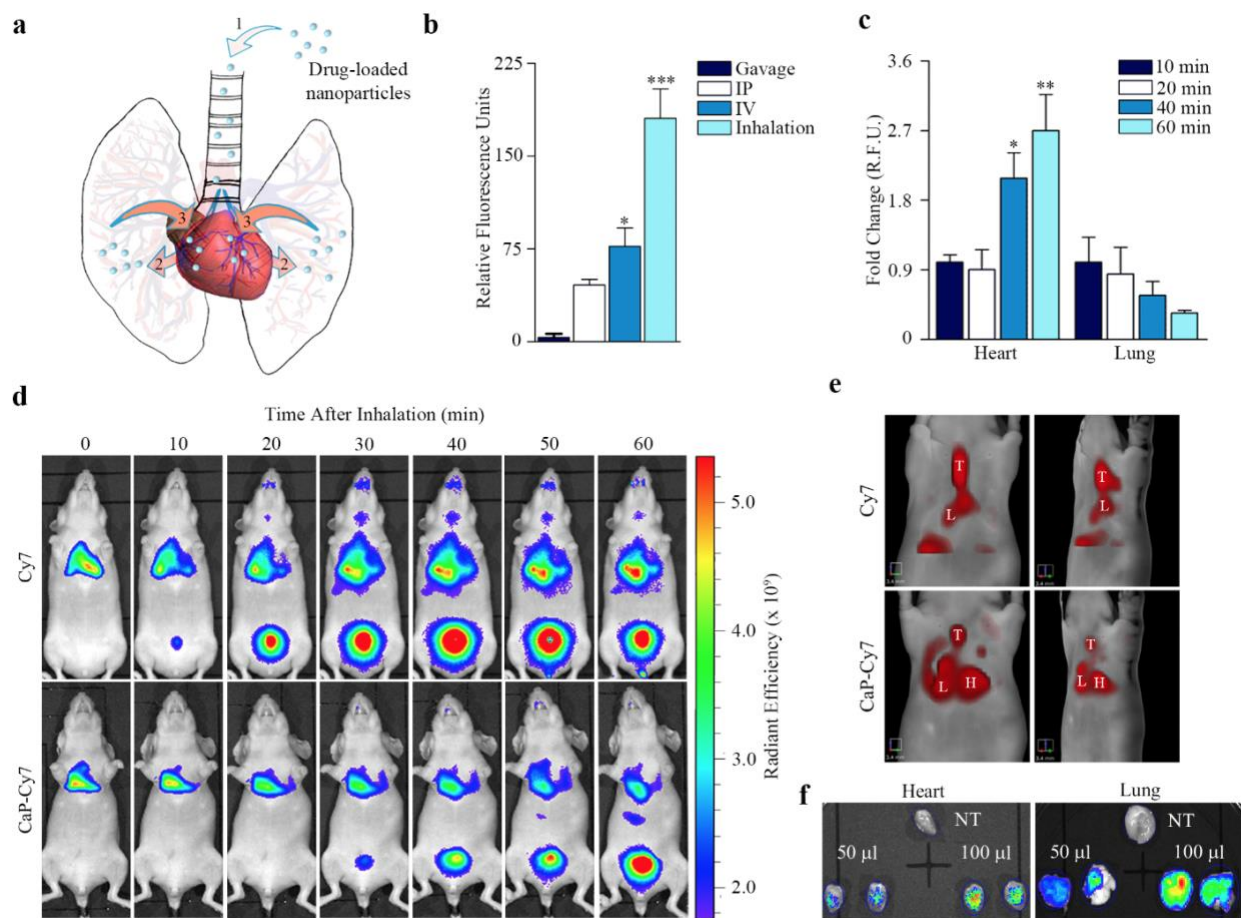


Fig. 1. Inhalation delivers CaPs to the heart. (a) Schematic representation of CaP heart targeting via the inhalation route. 1 = Nanoparticle inhalation; 2 = Nanoparticle deposition in lungs and translocation through the air-blood pulmonary barrier; 3 = Heart targeting and drug release into the heart. (b) Quantification of Cy7 fluorescence signals from heart tissue of mice treated with CaP-Cy7 via gavage, intraperitoneal (IP), intravenous (IV), and inhalation administration. All data are shown as mean \pm SEM * $P < 0.05$ and *** $P < 0.001$ compared to gavage (one-way ANOVA test) ($n = 5$). (c) Time-course quantification of Cy7 fluorescence signals from heart and lung tissue of mice treated with CaP-Cy7 via inhalation administration. All data are shown as mean \pm SEM * $P < 0.05$ and ** $P < 0.01$ compared to the 10 min time point (two-way ANOVA test) ($n = 5$). (d) Whole body optical *in vivo* imaging to evaluate the

distribution of CaP-Cy7 and Cy7 in CD1 nude mice at different time points after inhalation. Data are representative of at least 6 independent experiments. (e) 3D Fluorescence Molecular Tomography (FMT) imaging of mice as presented in d and analyzed 60 min post CaP-Cy7 and Cy7 administration. T = trachea, H = heart, L = lung. (f) Fluorescence imaging of explanted hearts from perfused mice analyzed 60 min post 50 and 100 μ l inhalation of CaP-Cy7. NT = heart from non-treated mouse.

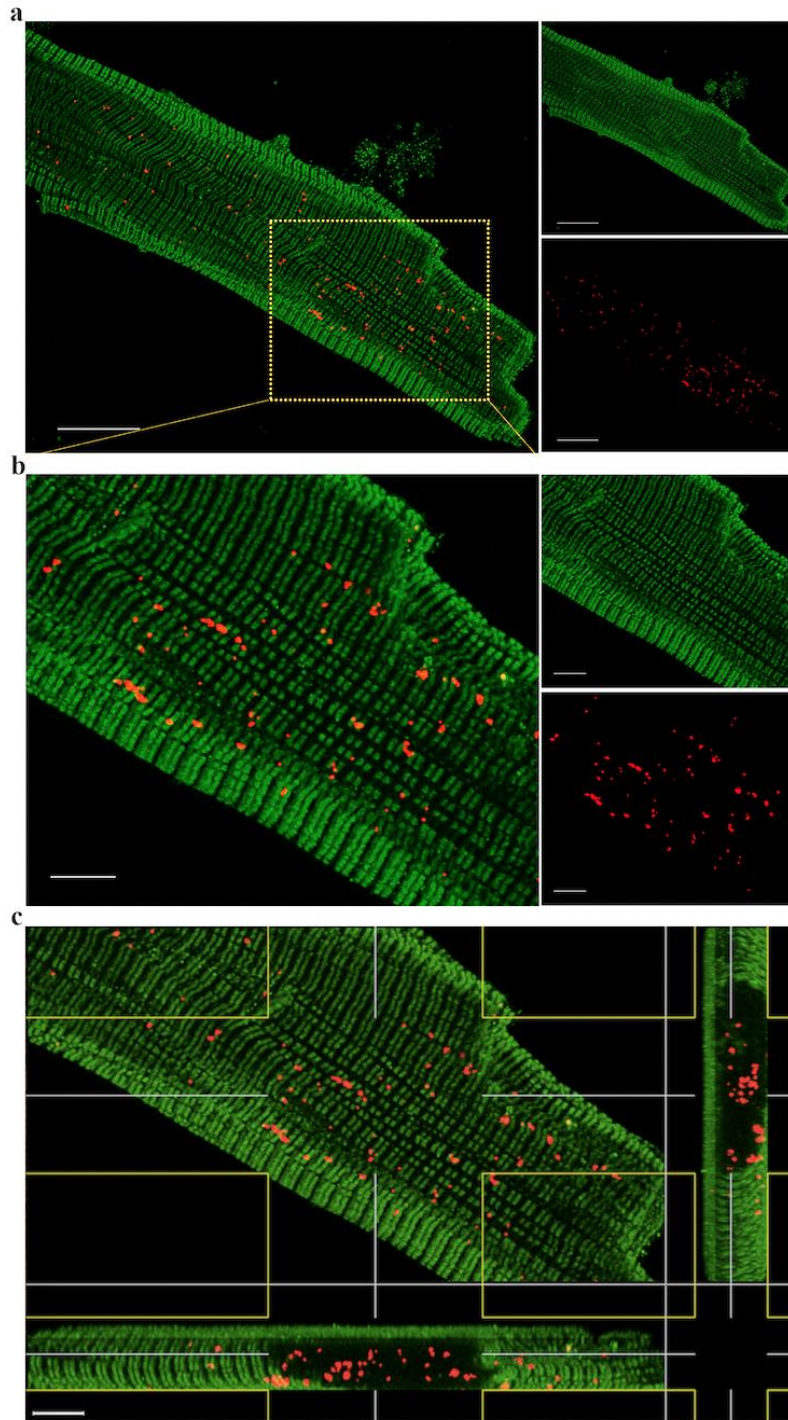


Fig. 2. Stimulated emission depletion (STED) microscopy of isolated cardiomyocytes from mice treated with MP-Rhodamine-loaded CaPs. (a) STED microscopy on an isolated cardiomyocyte from mice treated with MP-Rhodamine-loaded CaPs. Green: LTCC; Red: MP-

Rhodamine. Representative of 10 different acquisitions. Original magnification: 100X; Scale bar = 15 μ m. **(b)** Enlargement of yellow dotted-line squared shown in panel a. Scale bar = 5 μ m. **(c)** Orthogonal view of isolated cardiomyocyte shown in panel a and b. Original magnification: 100X; Scale bar = 5 μ m.

streptozotocin (STZ)-treated mice treated as indicated. All data are shown as mean \pm SEM ***P < 0.001 compared to NT mice (two-way ANOVA test) (n = 10). (c) Western blot analysis for the LTCC pore unit (Ca_v α 1.2) in adult cardiomyocytes isolated from treated mice. (d) Average peak of LTCC current density as a function of voltage command measured in adult cardiomyocytes isolated from treated mice. All values are shown as mean \pm SD for n cells *P < 0.02, NT compared to MP and CaP-HA mice (n = 16-21). (e) Contractility in adult cardiomyocytes isolated from treated mice. All data are shown as mean \pm SEM *P<0.05 and ***P < 0.01 compared to NT mice (two-way ANOVA test) (n = 20). (f) Z-stack confocal laser scanning microscopy images showing HA peptide in myocardial tissue from mouse treated with CaP-HA inhalation. Immunofluorescence staining for HA (Red), LTCC (green), and cell nuclei (DAPI, blue). Bar = 20 μ m, (n = 3).

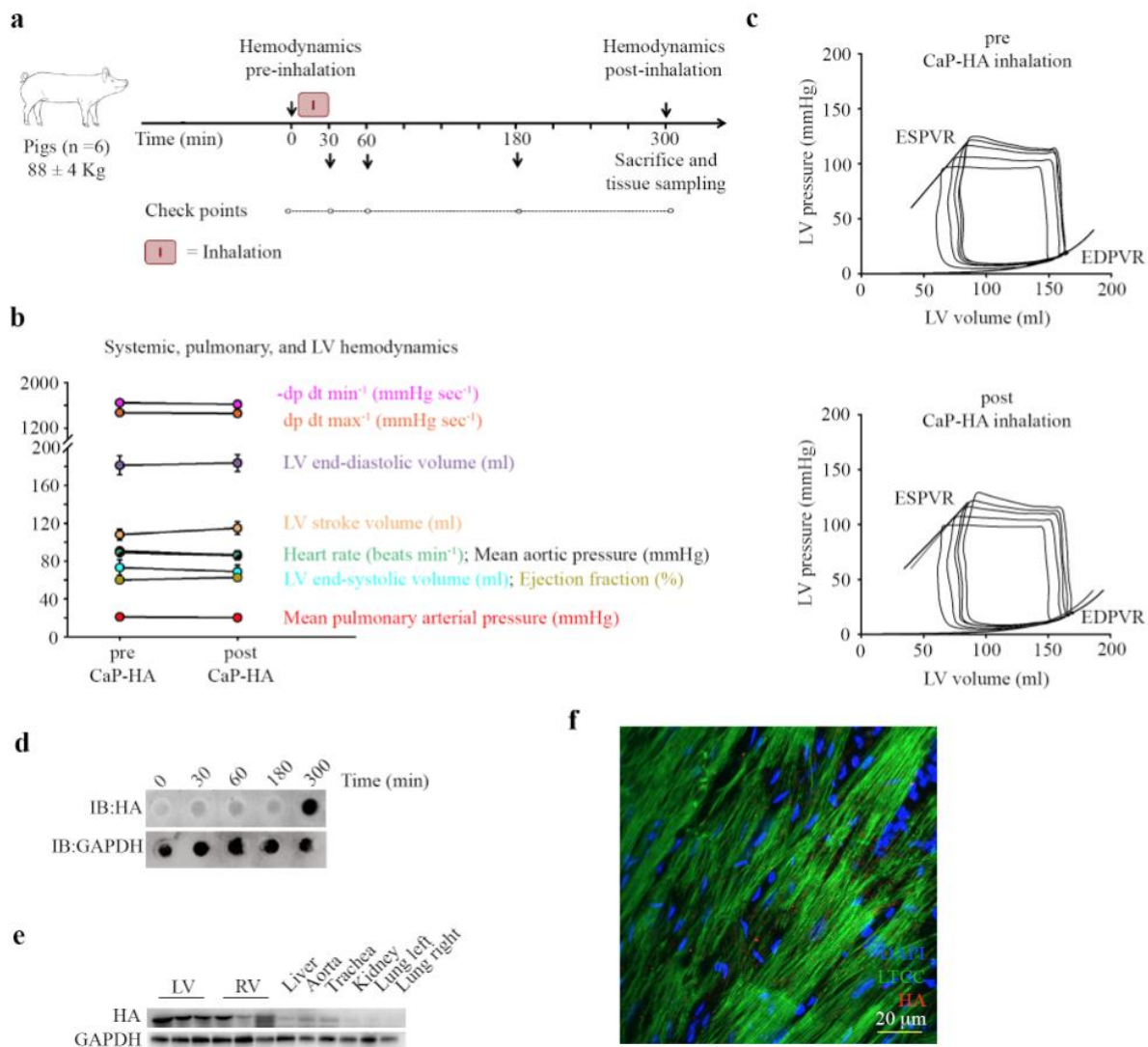


Fig. 4. CaP-HA inhalation in landrace pigs. (a) Design of the study. (b) Systemic, pulmonary and left ventricular hemodynamics (n = 6). (c) Original registrations of left ventricular pressure-volume loops before and after CaP-HA Inhalation. All registrations were recorded at spontaneous heart rate. ESPVR: end-systolic pressure-volume relationship. EDPVR: end-diastolic pressure-volume relationship. (d) Kinetics of inhaled CaP-HA cardiac targeting as examined by dot blot analysis from biopsies obtained at the indicated times. (e) Western blot analysis for HA on tissues of treated pigs. (f) Z-stack confocal laser scanning microscopy images

showing HA peptide in myocardial tissue from pigs treated with CaP-HA inhalation. Immunofluorescence staining for HA (Red), LTCC (green), and cell nuclei (DAPI, blue). Bar = 20 μm , (n = 3).

Author Contributions P.Ce., M.V., N.S., A.A., P.Ca., M.E., G.B.R., T.P., S.P., S.R., H.P., and M.M. carried out experiments. In particular, P.Ce., carried out several of the experiments and analyses; N.S., S.R., and M.M. were responsible for electrophysiology studies and analyses; M.V. performed all mouse setups and treatments, physiological analyses, and graphic representations; P.Ca. performed echocardiographic analyses and cardiomyocyte isolation; M.V. and M.E. performed *in vivo* imaging; M.E. performed STED; F.R and F.R. performed TEM on cardiac cells and tissue; H.P. and A.A. performed the large animal experiments; P.Ce., G.B.R., and T.P prepared and characterized nanoparticle formulations; S.P. and R.A. performed T-bars analysis; M.I designed and supervised the synthesis and functionalization of nanoparticles; M.M. and D.C. designed the study and supervised most of the experiments; M.M., M.I, G.C., and D.C. wrote the manuscript; A.T., H.P., M.M., M.I., and D.C. acquired funding for the study.

Supplementary Materials:

Supplementary Results

Material and Methods

Figures S1-S5

Movies S1-S3

Table S1-S6

References (1-10)

1. M. Giardiello, N. J. Liptrott, T. O. McDonald, D. Moss, M. Siccardi, P. Martin, D. Smith, R. Gurjar, S. P. Rannard, A. Owen, Accelerated oral nanomedicine discovery from miniaturized screening to clinical production exemplified by paediatric HIV nanotherapies. *Nature communications* **7**, 13184 (2016).
2. B. Y. Kim, J. T. Rutka, W. C. Chan, Nanomedicine. *The New England journal of medicine* **363**, 2434-2443 (2010).
3. M. E. Davis, J. E. Zuckerman, C. H. Choi, D. Seligson, A. Tolcher, C. A. Alabi, Y. Yen, J. D. Heidel, A. Ribas, Evidence of RNAi in humans from systemically administered siRNA via targeted nanoparticles. *Nature* **464**, 1067-1070 (2010).
4. V. Weissig, T. K. Pettinger, N. Murdock, Nanopharmaceuticals (part 1): products on the market. *International journal of nanomedicine* **9**, 4357-4373 (2014).
5. R. Kuai, L. J. Ochyl, K. S. Bahjat, A. Schwendeman, J. J. Moon, Designer vaccine nanodiscs for personalized cancer immunotherapy. *Nat Mater*, (2016).
6. Y. Zhao, F. Fay, S. Hak, J. Manuel Perez-Aguilar, B. L. Sanchez-Gaytan, B. Goode, R. Duivenvoorden, C. de Lange Davies, A. Bjorkoy, H. Weinstein, Z. A. Fayad, C. Perez-Medina, W. J. Mulder, Augmenting drug-carrier compatibility improves tumour nanotherapy efficacy. *Nature communications* **7**, 11221 (2016).
7. E. Blanco, H. Shen, M. Ferrari, Principles of nanoparticle design for overcoming biological barriers to drug delivery. *Nat Biotechnol* **33**, 941-951 (2015).
8. Y. T. Ho, B. Poinard, J. C. Kah, Nanoparticle drug delivery systems and their use in cardiac tissue therapy. *Nanomedicine* **11**, 693-714 (2016).
9. C. W. Evans, K. S. Iyer, L. C. Hool, The potential for nanotechnology to improve delivery of therapy to the acute ischemic heart. *Nanomedicine* **11**, 817-832 (2016).
10. S. S. Behera, K. Pramanik, M. K. Nayak, Recent Advancement in the Treatment of Cardiovascular Diseases: Conventional Therapy to Nanotechnology. *Current pharmaceutical design* **21**, 4479-4497 (2015).
11. S. Mendis, S. Davis, B. Norrving, Organizational update: the world health organization global status report on noncommunicable diseases 2014; one more landmark step in the combat against stroke and vascular disease. *Stroke; a journal of cerebral circulation* **46**, e121-122 (2015).
12. S. Suarez, A. Almutairi, K. L. Christman, Micro- and Nanoparticles for Treating Cardiovascular Disease. *Biomaterials science* **3**, 564-580 (2015).
13. K. Fosgerau, T. Hoffmann, Peptide therapeutics: current status and future directions. *Drug Discov Today* **20**, 122-128 (2015).
14. T. Uhlig, T. Kyprianou, F. G. Martinelli, C. A. Oppici, D. Heiligers, D. Hills, X. R. Calvo, P. Verhaert, The emergence of peptides in the pharmaceutical business: From exploration to exploitation. *EuPA Open Proteomics* **4**, 58-69 (2014).
15. V. Di Mauro, M. Iafisco, N. Salvarani, M. Vacchiano, P. Carullo, G. B. Ramirez-Rodriguez, T. Patricio, A. Tampieri, M. Miragoli, D. Catalucci, Bioinspired negatively charged calcium phosphate nanocarriers for cardiac delivery of MicroRNAs. *Nanomedicine* **11**, 891-906 (2016).
16. M. Savi, S. Rossi, L. Bocchi, L. Gennaccaro, F. Cacciani, A. Perotti, D. Amidani, R. Alinovi, M. Goldoni, I. Aliatis, P. P. Lottici, D. Bersani, M. Campanini, S. Pinelli, M. Petyx, C. Frati, A. Gervasi, K. Urbanek, F. Quaini, A. Buschini, D. Stilli, C. Rivetti, E. Macchi, A. Mutti, M. Miragoli, M. Zaniboni, Titanium dioxide nanoparticles promote arrhythmias via a direct interaction with rat cardiac tissue. *Particle and fibre toxicology* **11**, 63 (2014).
17. N. L. Mills, K. Donaldson, P. W. Hadoke, N. A. Boon, W. MacNee, F. R. Cassee, T. Sandstrom, A. Blomberg, D. E. Newby, Adverse cardiovascular effects of air pollution. *Nat Clin Pract Cardiovasc Med* **6**, 36-44 (2009).
18. M. Miragoli, P. Novak, P. Ruenaroengsak, A. I. Shevchuk, Y. E. Korchev, M. J. Lab, T. D. Tetley, J. Gorelik, Functional interaction between charged nanoparticles and cardiac tissue: a new paradigm for cardiac arrhythmia? *Nanomedicine* **8**, 725-737 (2013).
19. S. Bakand, A. Hayes, F. Dechsakulthorn, Nanoparticles: a review of particle toxicology following inhalation exposure. *Inhal Toxicol* **24**, 125-135 (2012).
20. W. H. De Jong, P. J. Borm, Drug delivery and nanoparticles: applications and hazards. *International journal of nanomedicine* **3**, 133-149 (2008).
21. J. R. Roberts, W. McKinney, H. Kan, K. Krajnak, D. G. Frazer, T. A. Thomas, S. Waugh, A. Kenyon, R. I. MacCuspie, V. A. Hackley, V. Castranova, Pulmonary and cardiovascular responses of rats to inhalation of silver nanoparticles. *J Toxicol Environ Health A* **76**, 651-668 (2013).

22. L. Petrick, M. Rosenblat, N. Paland, M. Aviram, Silicon dioxide nanoparticles increase macrophage atherogenicity: Stimulation of cellular cytotoxicity, oxidative stress, and triglycerides accumulation. *Environ Toxicol* **31**, 713-723 (2016).
23. K. Lin, C. Wu, J. Chang, Advances in synthesis of calcium phosphate crystals with controlled size and shape. *Acta Biomater* **10**, 4071-4102 (2014).
24. F. Rusconi, P. Ceriotti, M. Miragoli, P. Carullo, N. Salvarani, M. Rocchetti, E. Di Pasquale, S. Rossi, M. Tessari, S. Caprari, M. Cazade, P. Kunderfranco, J. Chemin, M. L. Bang, F. Polticelli, A. Zaza, G. Faggian, G. Condorelli, D. Catalucci, Peptidomimetic Targeting of Cavbeta2 Overcomes Dysregulation of the L-Type Calcium Channel Density and Recovers Cardiac Function. *Circulation* **134**, 534-546 (2016).
25. J. S. Patton, C. S. Fishburn, J. G. Weers, The lungs as a portal of entry for systemic drug delivery. *Proc Am Thorac Soc* **1**, 338-344 (2004).
26. M. Irngartinger, V. Camuglia, M. Damm, J. Goede, H. W. Frijlink, Pulmonary delivery of therapeutic peptides via dry powder inhalation: effects of micronisation and manufacturing. *European journal of pharmaceuticals and biopharmaceutics : official journal of Arbeitsgemeinschaft fur Pharmazeutische Verfahrenstechnik e.V* **58**, 7-14 (2004).



Supplementary Materials for Methods

Inhalation of peptide-loaded nanoparticles improves heart failure

Michele Miragoli,^{1,2,3,7,†*} Paola Ceriotti,^{1,3,†} Michele Iafisco,⁴ Marco Vacchiano,¹ Nicolò Salvarani,^{1,3} Alessio Alogna,^{5,6} Pierluigi Carullo,^{1,3} Gloria Belén Ramirez-Rodríguez,⁴ Tatiana Patrício,⁴ Lorenzo Degli Esposti,⁴ Francesca Rossi⁷, Francesca Ravanetti⁸, Silvana Pinelli,² Rossella Alinovi,² Marco Erreni,^{1,9} Stefano Rossi,² Gianluigi Condorelli,^{1,3,9} Heiner Post,⁵ Anna Tampieri,⁴ & Daniele Catalucci,^{1,3,*}

correspondence to: michele.miragoli@humanitasresearch.it
daniele.catalucci@cnr.it

This PDF file includes:

- Extended data
- Materials and Methods

Extended data

Nanoparticle preparation and characterization

Calcium phosphate nanoparticles (CaPs) were prepared according to an optimized procedure reported in our previous work (*1*), keeping the molar ratio of the reactants constant and using a crystallization time of 5 min at 37 °C. Immediately after dialysis, CaPs showed round shaped morphology with diameters of about 20-50 nm, Z-averages of 129 ± 2 nm, polydispersity index (PDI) of 0.18 ± 0.10 , and surface charges of -32 ± 2 mV according to transmission electron microscopy (TEM), dynamic light scattering (DLS), and ζ -potential analyses, respectively. These values are in line with our report (*1*). Additionally, CaPs in aqueous suspension ($600 \mu\text{g ml}^{-1}$) were evaluated for their long-term stability and surface charge as well as Z-average measured by ζ -potential and DLS analyses as a function of time (fig. S1). No changes were found for the surface charge, which remained stable (-32 ± 3 mV) for the whole time of investigation indicating that no phase transformations or chemical

modifications occurred at this stage. On the other hand, the initial Z-average value of about 125 nm, which is in agreement with our previous data (1), was found to decrease to about 80 nm 2 days after storage at 4 °C. Thereafter, this value remained very stable with only small variations (± 10 nm) up to 8 days, which was our current time limit of investigation (fig. S1a). Such difference for Z-average between the two periods was attributed to a reversible aggregation occurred during dialysis probably due to the effect of osmotic pressure and desalting. To unequivocally demonstrate that this reversible aggregation was caused by dialysis, analyses were then performed after 2 consecutive days of dialysis. This evaluation led to a Z-average of 130-150 nm, which is similar to the one obtained for CaPs after 6 hours of dialysis. Based on this evidence, all further tests included in this work were carried out using un-aggregated CaPs obtained at 2 days post dialysis.

To evaluate the potential interaction of proteins with CaPs, nanoparticles were analyzed in aqueous suspension enriched with FBS 10% (v/v). As shown in fig. S1b, the Z-average of CaP average decreased from about 80 nm (in pure water) to about 32 nm indicating that serum proteins interacting with the nanoparticles improved the dispersion of CaPs. Thereafter, a gradual increase of the Z-average was registered, reaching a value of about 280 nm at 7 days. Finally, an increment of the Z-potential from -30 to -10 mV corroborated the expected surface interaction of CaPs with proteins. The most important forces involved in protein-nanoparticle interaction are expected to be of electrostatic nature (Van der Waals and Coulomb), which is associated with the charged groups exposed at the protein/nanoparticles interface. The same behavior has been already reported for other kinds of nanoparticles when exposed to various media enriched with 10% (v/v) FBS (2-6). On this regard, it is important to remark that the effect observed with our nanoparticles starts within a time-range that is subsequent the necessary time required for the inhaled CaPs to target the heart, which is in the first hours. This is in line with data in fig. S1a,b showing that, within

the first 8 hours, size and surface charge of CaPs in contact FBS do not significantly changed in respect of the pristine nanoparticles (size less than 50 nm and surface charge of about -30 mV).

In our previous study (1), CaPs were functionalized with different quantities of microRNA, revealing a slight increase in CaP size as a function of microRNA amount, while comparable values to those of microRNA-free CaPs were obtained for the surface charge and morphology. Here, we performed a similar evaluation and characterized the effect of dye and peptides on size and surface of loaded CaPs (*i.e.* CaP-Cy7, CaP-MP, and CaP-HA). Notably, since our approach is based on a universal nature inspired synthetic strategy, we found that the incorporation mechanism for Cy7, MP, and HA into CaPs was similar to the previously observed for microRNA. This mechanism consists of a first step of interaction in which, within a basic reaction environment (pH 8.5), the Ca^{2+} and/or PO_4^{3-} ions interact via a strong electrostatic interaction with the chemical groups (*i.e.* carboxylate, amine and sulfonic groups, etc.) of the analyzed biomolecules. In the case of Cy7, the sulfonic and amine groups could be mainly involved in this interaction whereas the negative charge of MP and HA, which at pH of the reaction have a calculated isoelectric point of 7.06 (7), generally interact with Ca^{2+} ions. Afterwards, the reaction of PO_4^{3-} with Ca^{2+} ions or *vice versa* triggers the nucleation of particles and their growth, resulting in the mineralization of biomolecules (*i.e.* creation of a matrix of mineral phase surrounding the biomolecule-rich nucleus). Along this process, citrate stabilizes the nanoparticles and modulates their growth, as previously reported (1), through its binding on the surface at the early stage of crystallization.

In line with our previous results obtained with microRNA (1), immediately post dialysis higher Z-average but similar surface charge was obtained for functionalized CaPs compared to peptide-free CaPs. CaP-MP and CaP-HA showed comparable values for PDI (0.20 ± 0.10 and 0.21 ± 0.10), and surface charges (-31 ± 2 mV and -32 ± 1 mV),

respectively, indicating that their surface is homogeneously covered with citrate. Z-averages for the functionalized CaP-MP and CaP-HA were 210 ± 6 nm and 220 ± 6 nm, respectively, where the effective interaction of peptides with CaPs might determine the slight difference in size in respect to peptide-free CaPs (*i.e.* 125 nm). Also in this case and for the same reasons reported above, the Z-average of CaP-HA and CaP-MP immediately after dialysis decreased in function of time, passing from about 200 nm to 90 nm after 2 days (fig. S1a). This value remained stable with small variation (± 10 nm) up to 8 days, which was our time limit of investigation. Consistently, also in this case the surface charge of the CaP-peptides (-31 ± 3 mV) did not change as a function of time. TEM images of CaP-MP and CaP-HA (fig. S2d) showed round shaped particles of approximately 20-50 nm in diameter. The selected area electron diffraction (SAED) patterns collected from the same CaPs (fig. S2d) demonstrated their amorphous nature due to the presence of diffuse rings rather than spots. In addition, energy dispersive X-ray spectrometry (EDS) spectra (fig. S2d) revealed that both CaP-MP and CaP-HA are mainly composed of calcium and phosphate. All these features are comparable with our previously prepared CaPs (1) and we therefore assume that the functionalized CaPs synthesized in this work have similar behavior towards cardiomyocytes and cardiac tissue.

To evaluate peptide loading, the protein assay was adopted to quantify the total MP in CaP-MP preparations. Additionally, to distinguish the amount of CaP-loaded MP from the possible CaP-free MP present in the preparations, peptide quantification was performed from both pellet (CaP-MP) and supernatant (CaP-free MP) fractions obtained from centrifugation of CaP-MPs. Finally, an acidic treatment (0.05M HCl, 4 hours) was adopted to completely dissolve CaP-MPs from both fractions thereby facilitating the total release and effective quantification of total MP. Same approach was performed for both the pre- and post-dialysis preparations and data compared to the theoretical maximum loading. As shown in Table S1,

MP loading from the pellet fraction (corresponding to the CaP-loaded MP) was in line with the theoretical value leading to the conclusion that CaP provides high loading capacity while keeping minimal the amount of unloaded peptide (CaP-free MP). To evaluate MP stability within nanoparticles, CaP-MPs were stored at room temperature and peptide quantification was performed following a time-dependent approach. In particular, aliquots from the stored solution were processed adopting the above described approach and used for the analysis of peptide. As shown in fig. S2a, no significant reduction of MP loading was found supporting the fact that CaP-MPs stably maintain its payload in an encapsulated state. Thereafter, following a time-dependent response to CaP dissolution in acidic conditions, we evaluated release kinetics of encapsulated peptide from nanoparticles. As shown in fig. S2b, a gradual release of MP from CaP-MPs was obtained showing an inverse relationship between the reduction of the pellet fraction (CaP-loaded MP) and increase supernatant fraction (CaP-free MP). These data are in line with results from Inductively Coupled Plasma Optical Emission Spectrometry (ICP-OES) analyses (fig. S2c) that, by measuring the cumulating Ca^{2+} ion release in physiologic (pH 7.4) and slight acidic (pH 5.5) condition, provides degradation rate of CaP and peptide-loaded CaP. Degradation rate and consequently peptide release is triggered by pH value. Interestingly, CaPs loaded with peptide are slightly more degradable than pristine CaPs due to a weak destabilizing effect of MP and HA on the particle structure.

The quantification of Cy7 incorporated in CaPs revealed an amount of loaded Cy7 of 1.40 ± 0.13 % w/w. To demonstrate the effective incorporation of the dye inside nanoparticles, an amount of Cy7 corresponding to that one effectively encapsulated was adsorbed post-synthesis to CaPs surface (0.85 ± 0.08 % w/w). The analysis of the surface charge of CaP-Cy7 at pH 7.4 revealed the presence of a single population with surface charge of about -20 mV while the CaPs with the dye adsorbed on their surface showed a double population with surface charge of about -34 mV and -6 mV attributed to naked CaPs and dye

coated CaPs (fig. S1c). These data demonstrated that when included during the synthesis of nanoparticles, Cy7 was effectively encapsulated within the CaPs. CaP-Cy7 did not show a release of dye (limit of detection of $1 \mu\text{g ml}^{-1}$) against an infinite sink in dialysis as well as in aqueous suspension enriched with 10% (v/v) of FBS within the time scale of the *in vivo* experiments (*i.e.* 1 hour). It is important to note that on a very long time scale Cy7 will be released due to CaP dissolution.

Materials and Methods

Nanoparticles preparation. CaPs were generated according to our previous work⁽¹⁾ through a biomineralization-inspired strategy consisting of mixing (1:1 v/v, 20 mL total) two aqueous solutions of (a) CaCl_2 (100 mM) + Na_3Cit (400 mM) and (b) Na_2HPO_4 (120 mM) for 5 min at 37 °C. pH was adjusted to 8.5 by adding 0.1M NaOH (0.1M). The mixed solution was kept in a water bath at 37 °C for 5 min. For conjugation with a fluorophore, Sulfo-Cyanine7 amine (Cy7, Lumiprobe GmbH, Germany) ($125 \mu\text{g ml}^{-1}$) was added, while for drug conjugation, scramble (HA) or mimetic peptide (MP) ($500 \mu\text{g ml}^{-1}$) (HA: DQPPSRRDERA; MP: DQRPDREAPRS. Genescript, USA) was added. To remove unreacted reagents, the CaP suspension was dialyzed for 6 hours across a cellulose dialysis membrane with a cut-off of 3,500 Da and immersed in 400 mL Milli-Q water followed by multiple water exchanges. The suspension was recovered and stored at 4 °C until further use. The final concentration of CaP suspensions was $600 \mu\text{gml}^{-1}$ in all cases. The final concentrations of Cy7 and peptides within the CaP suspension were $75 \mu\text{gml}^{-1}$ and $150 \mu\text{gml}^{-1}$, respectively. Surface decoration of CaPs with Cy7 was also tested by adding an aqueous solution of Cy7 to the CaP suspension (final concentration of $15 \mu\text{gml}^{-1}$ similar to the amount effectively encapsulated). The suspension was maintained overnight under shaking at 37 °C. After that, the un-adsorbed dye was removed by extensively washings by centrifugation.

Nanoparticles characterization. The amount of CaPs after dialysis was evaluated by freeze-drying the sample suspensions (5 aliquots of 1 ml) and weighting the solid content. The amount of HA and MP loaded on CaPs was detected using DC protein Assay (Bio-Rad) according to the manufacturer's. The amount of Cy7 loaded on CaPs was measured by UV-Vis spectrophotometer (Nanodrop One, Thermo Scientific, USA) ($\lambda=750$ nm; $\epsilon_{cy7} = 240600$ M⁻¹ cm⁻¹). The concentration of Cy7 was calculated as difference between the concentration of the initial solution and that of the supernatant after sample centrifugation at 5000 rpm for 15 min. Size distribution and surface charge of unloaded and loaded CaPs were evaluated by DLS (Zetasizer Nano Series, Malvern, UK) and ζ -potential (Zetasizer Nano analyzer (Malvern, UK) analysis, respectively. CaPs particle size was measured by backscatter detection ($\lambda = 630$ nm, $\theta = 173^\circ$) and reported as Z-average of hydrodynamic diameter of three measurements of 10 runs for 10 sec at 25°C. ζ -potential measurements through electrophoretic mobility were carried out using disposable folded capillary cells (DTS1061; Malvern, UK) at 25°C, suspending CaP in 10 mM HEPES buffer at pH 7.4. The ζ -potential was calculated from three separate measurements (100 runs each) in each case. Transmission electron microscopy (TEM) images were collected using a FEI Tecnai F20 ST microscope operating at 80 kV (fig. S2d). An aliquot of 20 μ l of nanoparticles suspension was placed on a carbon/formvar coated-copper grid for 5 min. The grid was then washed with ultrapure water and dried by manual blotting. Stability of CaP, CaP-MP, and CaP-HA in aqueous solution (600 μ gml⁻¹) starting immediately after dialysis was evaluated measuring the Z-average and the surface charge of the suspensions as a function of time (up to 8 days) at 4 °C by DLS and ζ -potential analysis. The stability of the unloaded CaP suspension 2 days after dialysis enriched with 10% (v/v) of fetal bovine serum (FBS, Sigma Aldrich) was also evaluated up to 7 days at room temperature by DLS and ζ -potential analysis. The degradation

of CaPs and CaPs-peptide at different pH values, was evaluated mixing 5 mg of freeze-dried nanoparticles with 10 ml of 0.1 M HEPES buffer solution (pH 7.4) or 10 ml of 0.1 M Acetate buffer solution (pH 5.5). At scheduled times and up to 24 h, 1 ml of the supernatant (that was well separated from the solid phase by 15 min of centrifugation at 5000 rpm) were removed for Ca²⁺ quantification and replaced with fresh buffer. Calcium, content was determined by Inductively Coupled Plasma Optical Emission Spectrometry (ICP-OES) using a 5100 spectrometer (Agilent Technologies, Santa Clara, USA).

To evaluate peptide loading, the DC protein Assay (Bio-Rad) was adopted according to manufacturer's instruction. Quantification for both the pre- and post-dialysis preparations was performed from both pellet (CaP-MP) and supernatant (CaP-free MP) fractions obtained from centrifugation (14 min at 20000g) of CaP-MPs. Before peptide quantification assay, both pellet and supernatant fractions were subjected to an acidic treatment (0.05M HCl, 4 hours) to completely dissolve CaP-MPs and facilitate the total release and effective quantification of total MP.

The release of Cy7 from CaP-Cy7 was tested against an infinite sink in dialysis transferring the particles into 3500 Da MWCO cellulose membrane dialysis tubes and dialyzed against water for 24 h with multiple water exchanges. At scheduled times, 10 µl of the supernatant (that was well separated from the solid phase by 15 min of centrifugation at 5000 rpm) were analyzed for dye quantification by UV-Vis spectrophotometer.

The release of Cy7 from CaP-Cy7 was also tested in aqueous solution (600 µg/ml) enriched with 10% (v/v) of fetal bovine serum (FBS). At scheduled times, ranging from 1 min to 24 h, 10 µl of the supernatant (that was well separated from the solid phase by 15 min of centrifugation at 5000 rpm) were analyzed for dye quantification by UV-Vis spectrophotometer.

Peptides. Peptides and Rhodamine-conjugated peptides were synthesized by GenScript (USA). MP = DQRPDREAPRS, HA = DQPPSRRDERA.

Western blot analyses. Protein expression was evaluated in total lysates by Western and dot blot analyses according to standard procedures. Samples were homogenized in RIPA buffer (150 mM NaCl, 10 mM Tris pH 7.2, 0.1 % SDS, 1% Triton-X100, 5 mM EDTA, 100 μ M Na₃VO₄, 10 mM NaF, and Protease inhibitor 1X (Thermo Fisher Scientific)), loaded onto a 4-10% acrylamide gel separated by electrophoresis, and transferred to a nitrocellulose membrane (Millipore). Antibodies against the following proteins were used: Ca_v α 1.2 (Abcam), HA (GenScript), GAPDH (14C10) (Cell Signaling Technology), Goat anti-mouse-HRP, Goat anti-rabbit-HRP, and Rabbit anti-Goat IgG HRP (Thermo Fisher Scientific). ECL (Millipore) was used for protein detection using a Chemidoc MP Imaging System (Bio-Rad). Densitometry analyses was performed using Image Lab software (Bio-Rad).

RNA isolation and quantitative real-time PCR (q-RT-PCR) analysis. Total RNA was isolated using PureZOL™ RNA Isolation Reagent (Bio-Rad) according to the manufacturer's protocol. cDNA was generated using the High-Capacity cDNA Reverse Transcription Kit (Thermo Fisher Scientific) and amplified by qRT-PCR using GoTaq® qPCR Master Mix (Promega). Relative expression analysis was performed using the $\Delta\Delta$ Ct method by normalization to *U6*. The following primers were used: CD11 Fw (GACTCAGTGAGCCCCATCAT), CD11 Rev (AGATCGTCTTGGCAGATGCT); IL1 Fw (GCCCATCCTCTGTGACTCAT), IL1 Rev (AGGCCACAGGTATTTTGTCTG); TNF Fw (AGGCAGGTTCTGTCCCTTTCACT), TNF Rev (GCCATTTGGGAACTTCTCATCCCT); IL6 Fw (AGTTGCCTTCTTGGGACTGA), IL6 Rev (CAGAATTGCCATTGCACAAC); IL4 Fw (CATCGGCATTTTGAACGAG), IL4 Rev (CGAGCTCACTCTCTGTGGTG); IL5

Fw (ACATTGACCGCCAAAAACAG), IL5 Rev (ATCCAGGAACTGCCTGTC); U6 Fw (TTCACGAATTTGCGTGTTCAT), U6 Rev (CGCTTCGGCAGCACATATAC); Gapdh Fw (GGTCACCAGGGCTGCCATTTG), Gapdh Rev (TTCCAGAGGGGCCATCCACAG); Cacna1c Fw (GCAGCAGCTTTGCTGTCTTC), Cacna1c Rev (TGATCCGACCCTTGGCTTCA).

Thiobarbituric acid reactive substance detection (TBARS). TBARS were assessed as previously described (8). Briefly, tissue samples were extracted, washed in phosphate buffered saline (PBS) and included in cryovials prior to freezing at -80°C . Frozen tissue samples were homogenized and sonicated in PBS supplemented with protease inhibitor cocktail (Sigma-Aldrich, St. Louis, MO, USA). Insoluble debris was pelleted and lipid peroxidation products were detected in the supernatants, based on the condensation of malondialdehyde derived from polyunsaturated fatty acids, with two equivalents in order to give a fluorescent red derivative. 300 μl of tissue supernatant was mixed with an equal volume of 0.2 mol orthophosphoric acid and 1/16 volume of thiobarbituric acid in 0.1M NaOH and incubated at 90°C for 45 min. TBARS were extracted with n-butanol/NaCl and after centrifugation fluorescence was measured using a Cary Eclipse fluorescence spectrophotometer (excitation: 515 nm, emission: 545 nm). Malondialdehyde was used as standard for the calibration curve. TBARS concentrations were normalized to total protein concentration in each sample as determined using the BCA (bicinchoninic acid) Protein Assay (Thermo Scientific, Rockford, IL, USA). In parallel, TBARS concentrations were evaluated in plasma samples.

Confocal Microscopy. For immunostainings, fixed hearts were saturated in 10% and 30% sucrose in PBS and subsequently frozen in OCT, whereafter 10 μm cryosections were cut.

The slides were blocked and permeabilized with 3% normal goat serum, 0.3% Triton X-100 and 50 mM glycine in 1 x PBS for 1 hour. After incubation with primary and secondary antibodies, slides were scanned with an Olympus FluoView FV1000 confocal laser scanning microscope. Images were analyzed using Fiji Image J software (National Institutes of Health).

For stimulated emission depletion (STED) microscopy, cells were fixed on a cover glass (thickness #1.5) with 4% PFA for x 10 min, blocked, and permeabilized with 3% normal goat serum, 0.1% Triton X-100 in 1 x PBS for 1 hour. Cav α 1.2 (Abcam) was used as primary antibody while Alexa Fluor 488 goat anti-Mouse (Life Technologies) was used as secondary antibody. Mimetic peptide was conjugated to tetramethylrhodamine (TMR) as previously described. Mowiol [33% glycerol, 13% Mowiol powder (Calbiochem) 0,13M Tris buffer] was used as mounting medium. STED xyz images were acquired with a Leica SP8 STED3X confocal microscope system. AlexaFluor 488 was excited with a 488nm Argon Laser and emission was collected from 507 to 614 nm, while TMR was excited with a 545/547 nm-tuned white light laser (WLL) and emission was collected from 555 to 647 nm. Sequential acquisition was applied to avoid fluorescence overlap. A 660 nm CW-depletion laser was used for both excitations. Images were acquired with a Leica HC PL APO 100x/1.40 oil STED White objective. CW-STED and gated-STED were applied to the AlexaFluor 488 nm fluorophore and TMR, respectively. Collected images were de-convolved with Huygens Professional software and analyzed using Imaris 7.4.2 software (Bitplane).

Cy7 detection. Cy7 signal detection *ex vivo* was performed using a Synergy 4 instrument (BioTek) as described by the manufacturer.

Transmission Electron Microscopy analysis. CaP presence in the cardiac cells or tissue was analyzed by TEM microscopy in a JEOL JEM-2200 FS microscope (Tokio, Japan) operated at 80 KV. Briefly, we imaged cardiac tissue derived from Langerdoff-retroperfused mice hearts or isolated mouse cardiomyocytes as described below. Both tissue and pellet of cells were fixed in 2.5% glutaraldehyde / 0.1M PBS buffer pH 7.2 for 1 hours and then dehydrated through the graded series of acetone and embedded in Durcupan (Fluka Chemie, Buchs, Switzerland). The polymerization occurred after 24 hours at 65°C. Sections of 2 μ m were prepared using ultramicrotome Reichert (PabischWien), colored with Toluidine blue 0.5% sodium carbonate, and observed under light microscope. Ultrathin sections (~ 70 nm) were cut with a diamond blade, gathered on slotted copper grids, stained with uranyl acetate replacement stain (Electron Microscopy Science, PA, USA) and lead citrate. The micrographs were analyzed by ImageJ- Fiji software 1.51a.

Patch-clamp recordings. Adult cardiomyocytes derived from control and diabetic mice treated with nebulized nanocarriers were voltage-clamped in the whole-cell configuration (Multiclamp 700B, Axon Instruments) of the patch-clamp technique. In short, adult mouse ventricular myocytes were isolated and used within 3 hours from isolation. The cardiomyocyte suspension was placed in a chamber on the stage of an inverted microscope (Nikon eclipse, Ti), superfused at 1.5 ml/min and experiments were performed at room temperature ($24 \pm 2^\circ\text{C}$). Pipette resistances ranged from 1 to 3 M Ω and pipette potentials were zeroed before cell contact. Liquid junction potential corrections of 5 mV calculated using pCLAMP software (Axon Instruments) were applied before experiments. Signals were low-pass filtered (2.8 kHz), digitized (50 kHz), and stored for offline analysis. Data acquisition and analyses were performed using dedicated software (Axon pClamp 10 and Clampfit 10.3; Molecular Devices). Membrane capacitance (C_m) and series resistance (3–8

M Ω) were measured in every cell and compensated between 70% and 90% before LTCC current measurement, and the estimated voltage error was <5 mV in all cases. To take into account the variations in cell size, current amplitude was normalized to C_m and expressed as current density (pA/pF). Potassium currents were suppressed by substituting K⁺ with Cs⁺ in both the extracellular and the patch pipette solution. The composition of the extracellular solution was (in mmol/l): NaCl 140, CsCl 5.4, MgCl₂ 1.25, CaCl₂ 2, HEPES 10, D-glucose 10, adjusted to pH 7.4 with NaOH. The patch pipette solution contained (in mmol/l): CsCl 120, EGTA 10, MgCl₂ 4, HEPES 10, 4 Na₂ATP 4, adjusted to pH 7.4 with CsOH.

LTCC *I-V* relations were obtained by measuring activated current at different test potentials (400 ms; -50mV to 70mV at a rate of 0.33 Hz) from a holding potential of -90 mV; steady state activation curves were derived from each *I-V* relation. Steady-state inactivation curves were obtained by measuring the current activated at 10 mV after preconditioning voltage steps (1 sec) from -50 to 30 mV and normalizing it to the maximal current. In order to study LTCC current without contamination of Na⁺ current (*I*_{Na}) and T-type Ca²⁺ current (*I*_{Ca,T}) (if present), a 50-ms prepulse to -40 mV was used to inactivate both *I*_{Na} and *I*_{Ca,T}. Activation and inactivation curves were described by fitting experimental points with the Boltzmann equation to estimate the voltages of half-maximal activation and inactivation (*V*_{1/2}) and each slope-1 factor (*k*). Statistical comparisons were made using Student's t-test for unpaired samples. Data were obtained from > 3 different mice for each experimental condition. Differences with P<0.05 were regarded as significant.

Experimental Animals. *Mice.* All procedures on mice were performed according to institutional guidelines in compliance with national (D.L. 04/03/2014, n.26) and international law and policies (directive 2010/63/EU). The protocol was approved by the Italian Ministry of Health. Special attention was paid to animal welfare and to minimize the number of

animals used and their suffering. All experiments were performed on 10-week-old C57B6J male mice, CD1 male mice, and CD1- Foxn1 nude mice. All animals were obtained from Charles River Laboratories. Therapeutic treatment of mice was performed as follows: Type-1 diabetes was induced in adult C57B6/J male mice by intraperitoneal injection of streptozotocin (STZ, 50 mg/kg per day) for 5 consecutive days as previously described(9). 7 days after the last STZ injection, whole blood was obtained from the mouse tail vein and glucose levels were measured using the Accu-check Aviva blood glucose monitoring system (Roche). Mice were fasting for 8 hours before blood collection. At 3 weeks post STZ-treatment, mice were considered diabetic and used for the study only if glucose >250 mg/dL and %FS < 35% (29 out of 36 STZ-treated mice were considered suitable for the study). STZ diabetic mice were randomly divided in three separate groups and 50 µl solution (CaP-MP: 0.5 mg/kg/day; CaP-HA: 0.5 mg/kg/day; or MP: 0.5 mg/kg/day) was administered by inhalation via intratracheal nebulization for ten consecutive days as indicated.

Rats. The study population consisted of five male Wistar rats bred in the animal facility at the University of Parma, aged 12-14 weeks and weighing 300-350 g. Briefly, animals were anesthetized by intraperitoneal injection with a mixture of 40 mg/kg ketamine chloride (Imalgene, Merial, Milano, Italy) and 0.15 mg/kg medetomidine hydrochloride (Domitor, Pfizer Italia S.r.l., Latina, Italy). All efforts were made to minimize suffering. This study was carried out in accordance with the recommendations in the Guide for the Care and Use of Laboratory Animals of the National Institute of Health. The protocol was approved by the Veterinary Animal Care and Use Committee of the University of Parma and conforms to the National Ethical Guidelines of the Italian Ministry of Health (Permit number: 59/2012).

Landrace pigs. The experimental protocol was approved by the local bioethics committee of Berlin, Germany (G 0063/16), and conforms to the Guide for the Care and Use of Laboratory Animals published by the US National Institute of Health (NIH Publication No. 85-23,

revised 1996). A total of nine healthy animals were anaesthetized as previously described (10). Briefly, after administration of 1 mg/kg propofol, the animals were intubated and anaesthesia was continued with 1-1.5% isoflurane, 20 µg/kg/hour fentanyl and 0.2 mg/kg/hour pancuronium. The animals were ventilated (Cato® Dräger medical, Germany) with an FiO₂ of 0.5, an I:E-ratio of 1:1.5, a positive end-expiratory pressure of 5 mmHg, and a tidal volume of 10 ml/kg. The respiratory rate was adjusted continuously to maintain an end-tidal carbon dioxide partial pressure between 35 and 40 mmHg. Sheath accesses of the left internal carotid artery and jugular vein were surgically prepared. Heart rate and arterial blood pressure were continuously monitored. A balanced crystalloid infusion (Sterofundin ISO, B. Braun Melsungen AG, Melsungen, Germany) was administered at a fixed rate of 10 ml/kg/hour throughout the protocol. A body temperature of 37.5-38.5 °C was maintained by either surface cooling or a warming blanket.

Nanocarrier administration. *Mice.* CD1 mice were divided in four different groups of 6 mice and 100 µl of CaP-Cy7 were administered by gavage, intraperitoneal, and intravenous injection (Cap-IP) as well as by intratracheal nebulization. For the intratracheal treatment MicroSprayer® Aerosolizer – Model IA-1C and a FMJ-250 High Pressure Syringe (Penn-Century™) was used. Mice were anesthetized with 3% isoflurane to allow the nebulization. For each administration method, 11 mice administered with an aqueous Cy7 solution were used as controls. At the end of the experimentation, mice were sacrificed and tissues collected.

Rats. Administration was performed via a 16-gauge catheter connected to a rodent ventilator (Rodent ventilator UB 7025, Ugo Basile, Comerio, Italy) for artificial respiration. One dose of 20 µl/100 g BW solution (3 mg/kg CaP-NP or saline) was administered via the. After CaP-NP administration, the animal was woken up with a single intraperitoneal injection of 0.15

mg/kg atipamezole hydrochloride (Antisedan, Pfizer, Italy) and leaved conscious for four hours before performing electrophysiological *in vivo* experiments. Before exposing the heart, pre-cordial ECGs (3 unipolar and 3 bipolar leads) were recorded in order to screen for possible anoxic effects on cardiac electrical activity due to the tracheal instillation (data not shown).

Landrace pigs. A left lateral thoracotomy was performed and the left ventricle was exposed in a pericardial cradle. The protocol is described in fig. 5a. After stabilisation for 30 min, two transmural left ventricular biopsies were taken from the beating heart. Next, a 10 ml solution containing 10 mg/ml CaP-HA (150 µg/ml HA) was nebulized over 30 min with the Aeroneb Professional Nebulizer System (Aeroneb Pro, Aerogen Ltd., Galway, Ireland), connected with an adult T-piece into the inspiratory limb of the breathing hoses. At 30, 60, 180, and 300 min after the beginning of inhalation, further biopsies were taken. All biopsies were rinsed carefully in saline, immediately frozen in liquid nitrogen, and stored at -80 °C. Finally, the animals were sacrificed by a bolus injection of 100 mmol potassium chloride and samples from plasma, trachea, lung, heart, liver, kidney and descending aorta were collected.

Cardiomyocyte contractility measurements. Measurements of cardiomyocyte contractility were carried out as previously described (9). Briefly, cardiomyocytes were placed in a perfusion system and continuously perfused with a standard Tyrode solution containing 1.2 mM Ca²⁺. Cells were field stimulated at increasing frequencies (from 0.5 to 2 Hz) as described in the result section and sarcomere length was recorded. Data were analyzed using Ion Wizard software (IonOptix Corp., Milton, USA).

Echocardiography. A Vevo 2100 high-resolution *in vivo* imaging system (VisualSonics Fujifilm) with a MS550S probe "high frame" scanhead was used for echocardiographic analysis. Mice were anesthetized with 1.0% isoflurane and imaged in the M-mode as previously described (9).

***In vivo* epicardial potential mapping.** *In vivo* epicardial potential mapping was performed as previously described (9). Briefly, treated animals were anesthetized by intraperitoneal injection of a mixture of 40 mg/kg ketamine and 0.15 mg/kg medetomidine, and ventilated at ~85 cycles per minute. Subsequently, the heart was exposed through longitudinal sternotomy and an epicardial electrode (EE) array (8×8 with a 1 mm resolution square mesh) was used to record unipolar epicardial electrograms during sinus rhythm and ventricular pacing. Cardiac excitability and refractoriness as measures of susceptibility to arrhythmias were evaluated.

***In vivo* imaging.** CD-1 nude mice (from Charles River Laboratories) were fed with AIN-76A alfalfa-free diet (Mucedola srl) for two weeks in order to reduce fluorescence background. At the time of acquisition, CD-1 nude mice were anesthetized with ketamine and xylazine and solutions containing CaP-Cy7 or Cy7 alone were nebulized intratracheally using a Penn-Century™. Fluorescence images were acquired with an IVIS Lumina III imaging system (Perkin Elmer). The following acquisition parameters were used: excitation filter range: 680 to 740 nm, emission filter: 790 nm, exposure time: 2 sec, binning factor 4, and f/Stop: 2. Images were acquired every 10 minutes for 1 hour. Uninjected mice were used as background. Spectral unmixing, image processing, and analysis were performed using Living Image 4.3.1 software (Perkin Elmer). For Fluorescence Molecular Tomography (FMT) imaging, mice were placed in a dedicated imaging cassette and imaged in three-dimensions

using the FMT2000 imaging system (Perkin Elmer). Acquired images were subsequently processed using TrueQuant 3.1 software (Perkin Elmer). At the end of the experiment, mice were sacrificed and organs collected for *ex vivo* imaging using an IVIS Lumina III imaging system (Perkin Elmer). Spectral unmixing, image processing, and analysis were performed using Living Image 4.3.1 software (Perkin Elmer).

Invasive hemodynamics in Landrace pigs. A separate series of pigs (n=6, 88±4 kg, Fig.4a) were acutely instrumented closed-chest under fluoroscopic guidance with a pulmonary artery flotation catheter (Edwards Lifesciences CCO connected to Vigilance II, Edwards Lifesciences, Irvine, CA), a LV conductance catheter (5F, 12 electrodes, 7-mm spacing; MPVS Ultra, Millar Instruments, Houston, TX), and a valvuloplasty catheter (24 mL; Osypka, Rheinfelden, Germany) in the descending aorta, as previously described (10). A 3-lead surface ECG was recorded throughout the whole experiment and used for offline analysis. Offline analysis included measurements of PQ intervals during spontaneous heart rates, QRS duration and QT duration. After stabilisation for 30 min, steady-state hemodynamics were acquired over three respiratory cycles. Pressure-volume relationships were generated by briefly inflating the intraaortic balloon catheter three times. Next, a 10 ml solution containing 10 mg/ml CaP-HA (150 µg/ml HA) was nebulized over 30 min with the Aeronex Professional Nebulizer System, as above described. Measurements were then repeated after 300 minutes. Pressure-volume data and time intervals were analyzed off-line by CircLab Software (custom made by Prof. P. Steendjik). The conductance catheter measurements were calibrated by hypertonic saline (3 boluses of 3 mL at 10%) and cardiac output continuously derived from the pulmonary artery flotation catheter.

Statistical Analysis. Assessment of normality of the data was calculated with the Kolmogorov-Smirnov (K-S) test. Statistical comparisons were performed using the one-way or two-way ANOVA test and Student's t-test for unpaired samples in Patch Clamp experiments. Prism 6.0 software (GraphPad Software, CA) was used to assess normality of the data and for statistical calculation. A P value < 0.05 was considered significant unless otherwise indicated.

Supplementary Figures

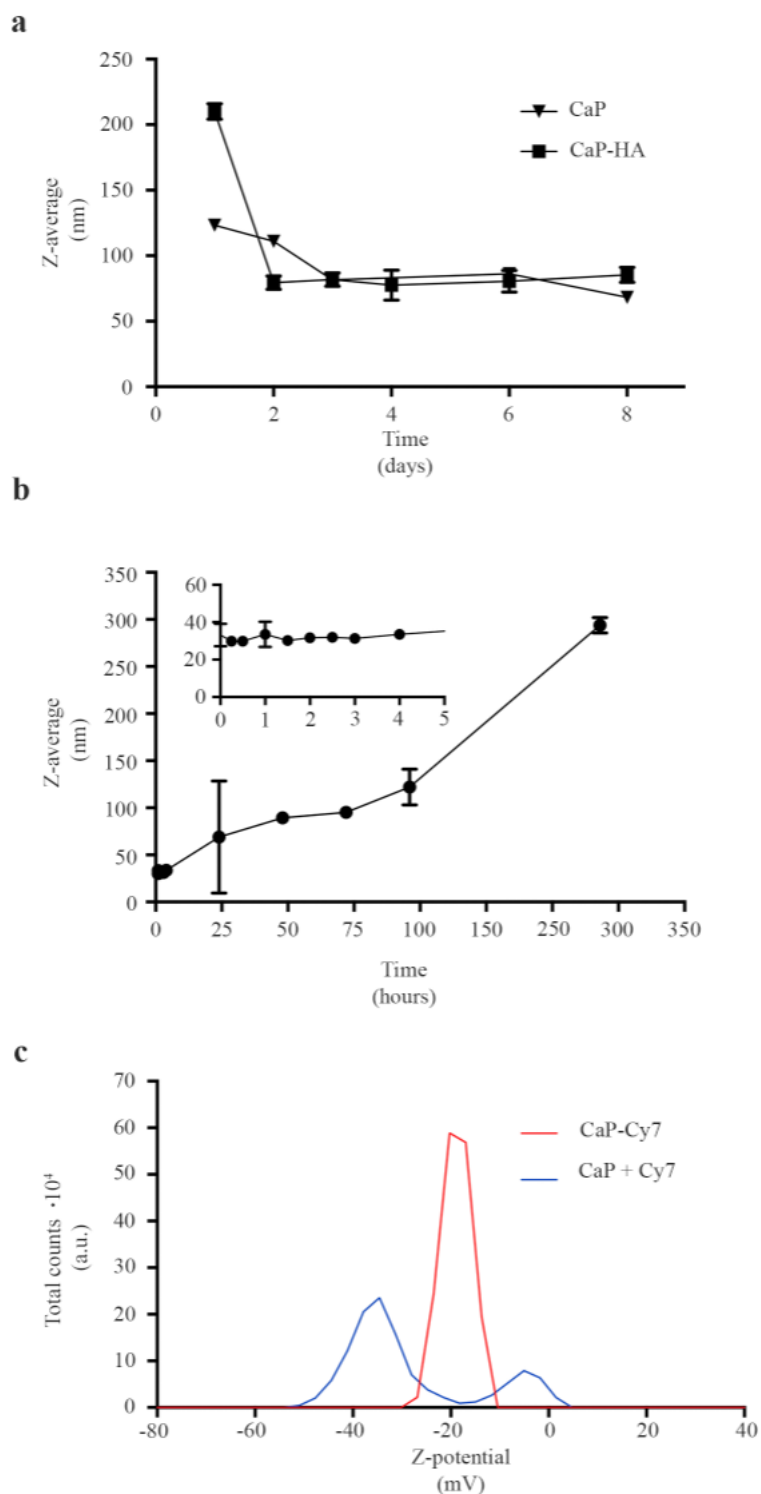


Figure S1: CaP size and charge characterization. **a**, Mean particles size (Z-average) as a function of time of pristine CaP and CaP-HA in water ($600 \mu\text{g ml}^{-1}$). Data points of CaP-MP were similar to those of CaP-HA and for the sake of clarity they were not included in the

graph. Results expressed as mean \pm S.E.M (n = 6). **b**, Mean particles size (Z-average) as a function of time of CaP in water ($600 \mu\text{g ml}^{-1}$) enriched with 10% (v/v) of FBS. The inset shows the data acquired in the short time scale. Results expressed as mean \pm S.E.M (n = 6). **c**, ζ -potential values at pH 7.4 of CaP-Cy7 and CaPs with Cy7 adsorbed on their surface (CaP +Cy7).

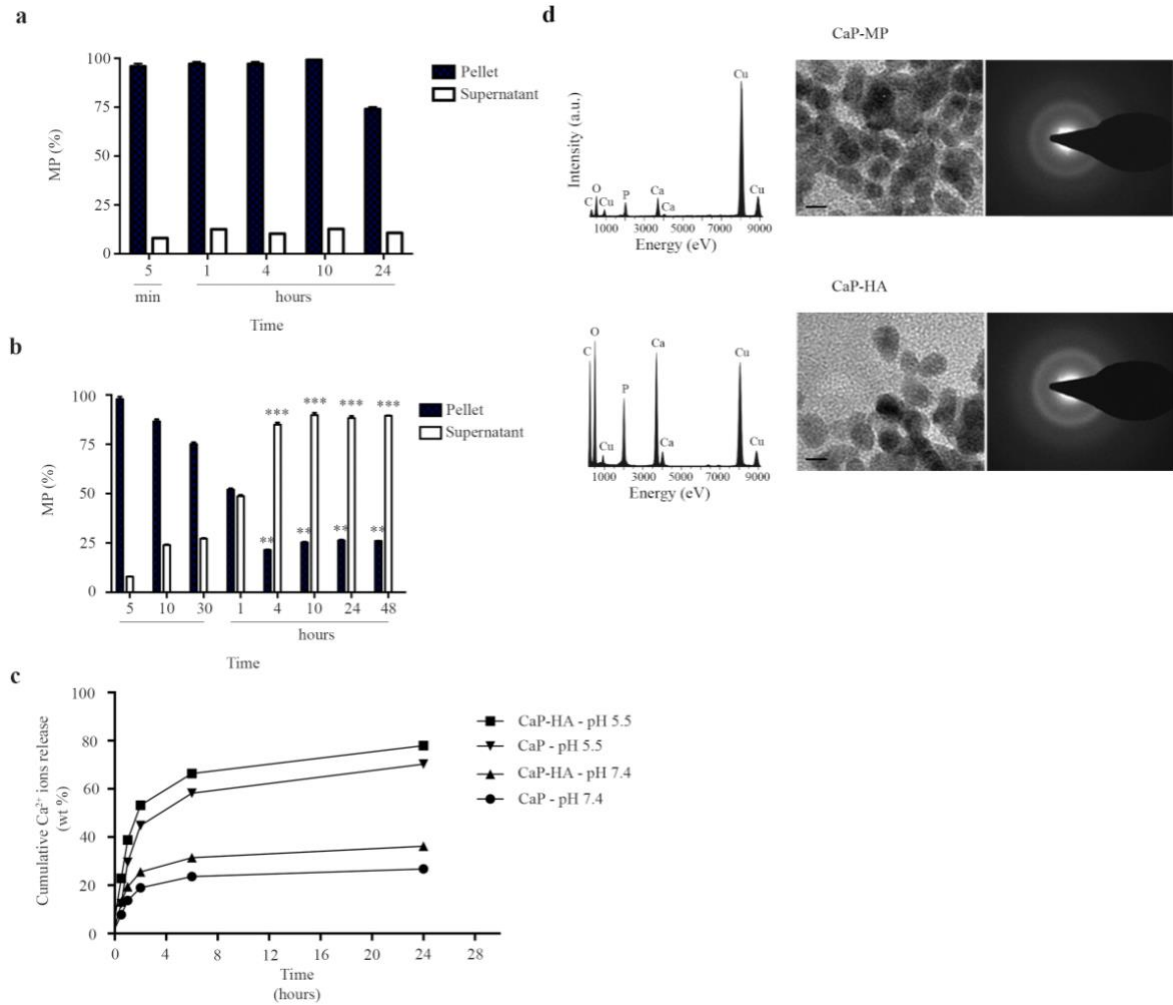


Figure S2: CaP stability, loading, and structure characterization. **a**, Stability of CaP-MP loading. Time-dependent release profile of MP from CaP-MP preparation. Data are expressed as average percentage over time and compared to the initial time point. Results expressed as mean \pm S.E.M, statistical significance was not obtained. (n = 6). **b**, MP release from CaP-MP. Time-dependent release profile of MP from acidic dissolution of CaP-MP preparation. Data are expressed as average percentage over time. **, P < 0.01, ***, P < 0.001 vs the initial time point of analysis. Results expressed as mean \pm S.E.M (n = 6) **c**, Cumulative release of Ca²⁺ ions (wt%) from CaP and CaP-HA at pH 7.4 and pH 5.5 as a function of time. Data points of CaP-MP were similar to those of CaP-HA and for the sake of clarity they were not included in the graph. Results expressed as mean \pm S.E.M (n = 6). **d**, Transmission Electron Microscopy (TEM) images and Selected Area Electron Diffraction (SAED) patterns of CaP-

MP (upper left) and CaP-HA (upper right), Scale bar 50 nm; Energy-Dispersive X-ray (EDX) spectroscopy of CaP-MP (bottom left) and CaP-HA (bottom right).

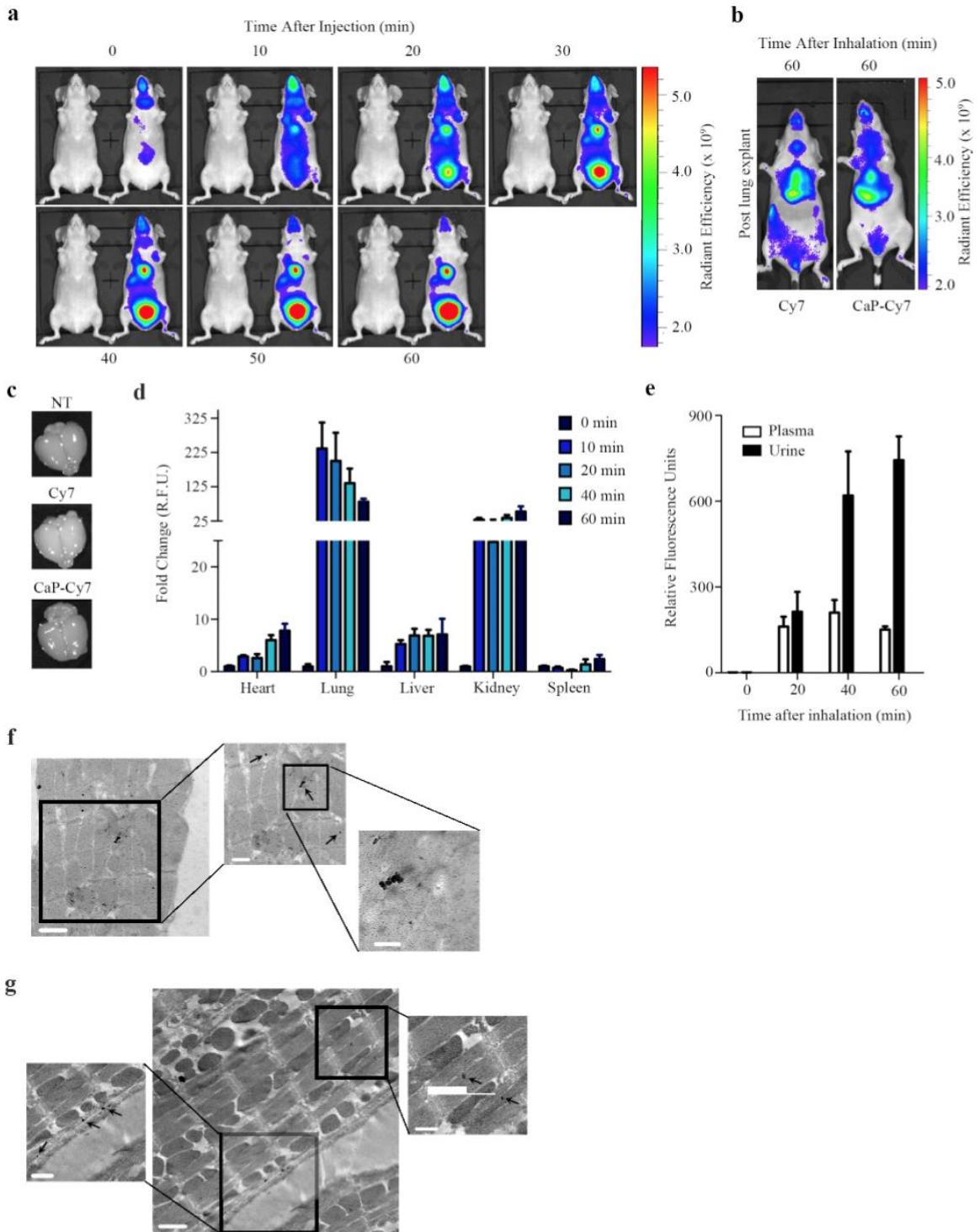


Figure S3: *In vivo* and *ex vivo* characterization of CaPs. a, *In vivo* fluorescence whole body imaging to evaluate the distribution of CaP-Cy7 and Cy7 in CD1 nude mice at different time points after retro-ocular injection. Data are representative of at least 6 independent experiments. b, *In vivo* fluorescence whole body imaging from the same mice as shown in

Figure 1d after lung explantation. **c**, Fluorescence acquisition from brains isolated from the same mice as shown in Figure 1d. Data are representative of at least 6 independent experiments. All data are shown as mean \pm SEM (n = 10). **d**, Time-course quantification of Cy7 fluorescence signals from tissue of mice treated with CaP-Cy7 via inhalation administration. Data are normalized per mg of tissue and refer to the initial time-point 0. All data are shown as mean \pm SEM *P < 0.05 and **P<0.01 compared to the first-time point (two-way ANOVA test) (n = 5). **e**, Time-course quantification of Cy7 fluorescence signals from plasma and urine samples of mice treated with CaP-Cy7 via inhalation administration. Data are normalized per volume and refer to the initial time-point 0. All data are shown as mean \pm SEM ***P<0.001 compared to the first-time point (two-way ANOVA test) (n = 5). **f-g**, Electron dense CaP-NPs from (f) isolated adult cardiac myocytes (administration of 50 ug/ml of CaP-NPs for 30 min) and (g) mouse heart. In f, arrows indicate the presence of isolated or aggregated CaP-NPs. In g, electron dense CaP-NPs are positioned in the myofibrils (right inset) and underneath the sarcolemma (left inset). Arrows indicate the presence of CaP-NPs.

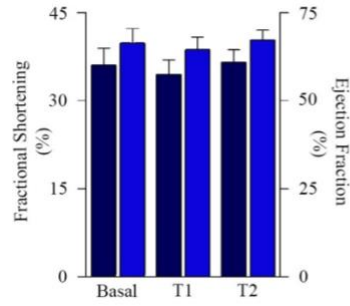


Figure S4: Echocardiographic analysis of CaP-treated mice. Fractional shortening (%; index of heart contraction) and ejection fraction (%; fraction of blood ejected from the left ventricle) as determined by echocardiographic analysis on healthy mice before and after treatment with CaP. FS (black), EF (blue).

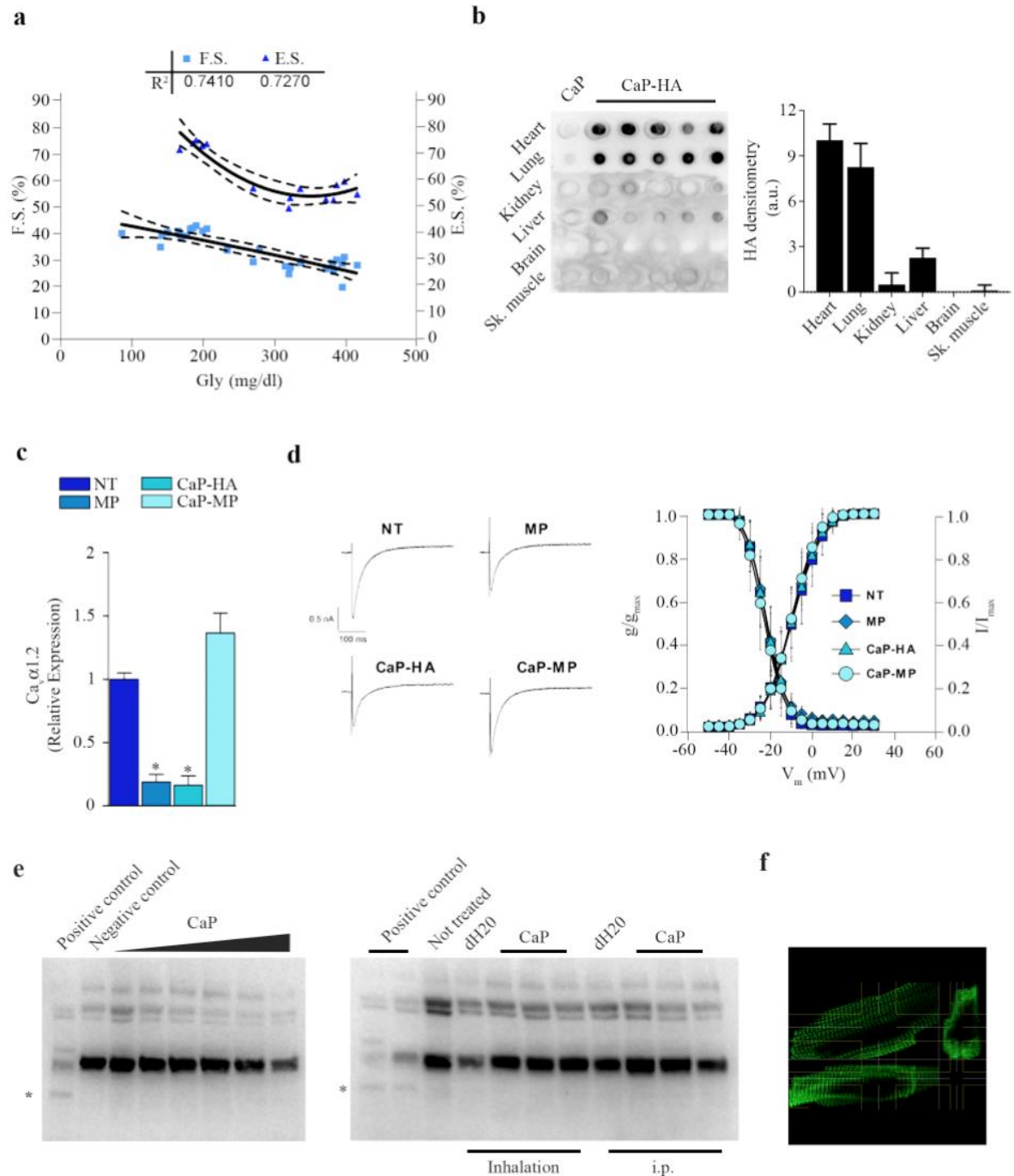


Figure S5: MP-CaP treatment of diabetic mice. **a**, Fractional shortening (%), ejection fraction (%) and glycaemia in diabetic mice. All data are shown as mean \pm SEM ($n = 10$). **b**, Representative image of dot blot analysis on protein lysates extracted 24 hours post last inhalation of CaP-HA- or CaP-treated mice ($n = 5$). **c**, qRT-PCR analysis for LTTC pore unit ($Ca_v\alpha_{1.2}$) expression on left ventricular RNA as indicated ($n = 12$). These data are in agreement with results obtained in our previous study(*1*), where R7W-MP administration

resulted in de-repression of Cav α 1.2 gene expression both *in vitro* and *in vivo*. **d**, Representative LTCC single current traces recorded at 5 mV (top), and LTCC steady-state activation/inactivation curves (bottom) measured in adult cardiomyocytes isolated from treated mice as shown in Fig. 3d. All values are reported as means \pm SD for n cells (n = 16-21). No statistical significance was observed. **e**, *Ex vivo* (left) and *in vivo* (right) effect of CaPs on complement activation. Left: Plasma from mice was incubated for 20 minutes with increasing amounts (0.25, 0.5, 1, 2, 4, 8 μ g) of CaPs and complement activation was monitored by Western blot analyses for C3 activation fragment (indicated with a *). Data indicate no presence of C3 fragment in any of the CaP treated samples indicating no complement activation. Positive control = bacterial lysate; NT = not treated. (n = 5). Right: 50 μ l of 500 μ g/ml CaP, corresponding to the single dose administered in all *in vivo* assays, were administered by inhalation or intraperitoneal injection to mice. 60 minutes post treatment, blood was collected and plasma subjected to Western blot analyses for C3 activation fragment (indicated with a *). Absence of C3 fragment in any of the CaP treated mice indicate no complement activation. Positive control = bacterial lysate. NT = not treated samples. (n = 3). **f**, Orthogonal view of isolated cardiomyocyte from mice treated with CaPs. Green: LTCC. Representative of 10 different acquisitions. **b**. Original magnification: 100X; Scale bar = 5 μ m.

Video S1. 3D Fluorescence Molecular Tomography (FMT) imaging of the cardio-pulmonary area from Cy7-treated mice. Mice were treated with Cy7 alone by inhalation and analyzed 60 min after administration. Representative of at least 5 different experiments.

Video S2. 3D FMT imaging of the cardio-pulmonary area from CaP-Cy7-treated mice. Mice were treated with CaP-Cy7 by inhalation and analyzed 60 min after administration. Representative of at least 5 different experiments.

Video S3. Stimulated emission depletion (STED) microscopy of isolated cardiomyocytes from mice treated with MP-Rhodamine-loaded CaPs. STED microscopy on a cardiomyocyte isolated from mice treated with MP-Rhodamine-loaded CaPs. Green: LTCC; Red: MP-Rhodamine. Representative of 10 different acquisitions. Original Magnification: 100X

Table S1: CaP-MP loading.

	PREPARATION 1				PREPARATION 2			
	PRE-DIALYSIS		POST- DIALYSIS		PRE-DIALYSIS		POST- DIALYSIS	
	theoretical	measured	theoretical	measured	theoretical	measured	theoretical	measured
CaP-MP	150	129 ± 2	120	135 ± 5	600	596 ± 11	480	396 ± 6
Pellet		173 ± 4		135 ± 9		528 ± 9		340 ± 4
Supernatant		0.65 ± 0.020		0.82 ± 0.010		1.4 ± 0.300		0.081 ± 0.001

Value are expressed as µg of MP per 500 µg of CaP.

Table S2: Echocardiographic analysis of 10-week-old male WT mice treated with CaP.

	Weight	IVSd	LVIDd	LVPWd	IVSs	LVIDs	LVPWs	FS	EF	HR
	(g)	(mm)	(mm)	(mm)	(mm)	(mm)	(mm)	(%)	(%)	(bpm)
Basal	25.0 ± 0.7	0.84 ± 0.04	3.41 ± 0.12	0.81 ± 0.08	1.22 ± 0.05	2.18 ± 0.23	1.17 ± 0.05	36.06 ± 6.40	66.38 ± 8.97	609 ± 35
1 Treatment	24.6 ± 0.6	0.91 ± 0.04	3.34 ± 0.20	0.81 ± 0.06	1.22 ± 0.08	2.19 ± 0.23	1.16 ± 0.08	34.46 ± 5.51	64.46 ± 7.95	601 ± 24
3 Treatments	24.2 ± 0.8	0.88 ± 0.04	3.41 ± 0.18	0.83 ± 0.03	1.23 ± 0.09	2.17 ± 0.25	1.20 ± 0.05	36.54 ± 4.17	67.20 ± 6.28	662 ± 34****

IVSd, interventricular septal thickness in diastole; LVIDd, left ventricular inner diameter in diastole; LVPWd, left ventricular posterior wall thickness in diastole; IVSs, interventricular septal thickness in systole; LVIDs, left ventricular end-systolic diameter in systole; LVPWs, left ventricular posterior wall thickness in systole; FS, left ventricular fractional shortening; EF, ejection fraction; HR, heart rate (n=5 per group). *** P<0.005 vs. Basal (Two-Way ANOVA)

Table S3: Excitability and refractoriness parameters obtained by epicardial multiple lead recording in untreated mice or mice treated with CaP.

	Rheobase	Chronaxie	ERP	P wave	QRS
	(μ A)	(ms)	(ms)	(ms)	(ms)
Control	28.9 ± 6.5	0.9 ± 0.2	73.5 ± 13.0	27.5 ± 0.4	15.6 ± 0.2
CaP	22.6 ± 4.5	1.2 ± 0.2	86.6 ± 13.4	29.7 ± 0.5	14.9 ± 0.1

ERP: effective refractory period.

Table S4: Thiobarbituric acid reactive substance detection in mice treated with MP, CaP-HA, and CaP-MP.

	LV			RV			Septum			Kidney		
	TBARS (nM)	Proteins (g/l)	TBARS/prot (nmoles/g)									
NT	429±125	6.75±3.99	80.66±43.61	663±109	3.64±1.69	212.07±96.90	507±112	4.69±2.66	131.90±63.52	154±114	29.60±11.56	5.57±3.66
MP	499±107	12.25±3.80	41.66±4.73	661±45	3.71±1.11	192.98±76.09	611±86	3.60±1.69	195.38±90.89	118±62	30.43±10.28	4.11±2.27
CaP-HA	485±197	7.82±1.60	65.69±37.04	563±184	3.08±0.50	188.97±76.22	586±141	4.54±1.08	134.74±47.89	91±54	26.88±5.47	3.75±2.91
CaP-MP	507±103	6.81±1.24	78.41±32.55	667±24	3.53±0.42	191.20±27.80	532±58	3.61±1.32	167.17±84.18	95±84	19.25±4.00	5.34±2.93

	Lung			Liver			Spleen			Serum
	TBARS (nM)	Proteins (g/l)	TBARS/prot (nmoles/g)	TBARS (nM)	Proteins (g/l)	TBARS/prot (nmoles/g)	TBARS (nM)	Proteins (g/l)	TBARS/prot (nmoles/g)	TBARS (nM)
NT	77±50	7.83±2.60	9.90±4.71	67±27	26.63±17.37	4.27±4.01	214±131	12.12±6.27	19.04±14.40	0.26±0.05
MP	37±10	4.80±0.87	7.87±2.09	72±25	18.75±11.75	5.27±3.46	122±62	7.33±2.01	19.41±15.96	0.24±0.02
CaP-HA	40±15	4.64±2.24	9.88±3.80	45±19	15.38±6.13*	3.65±3.02	128±79	4.38±2.63	29.46±12.44	0.23±0.02
CaP-MP	93±37	8.66±1.23	10.66±3.36	68±21	14.50±8.49*	6.19±4.41	168±69	8.17±2.33	23.55±16.56	0.25±0.04

LV, left ventricle, RV: right ventricle; NT, not treated; MP, mimetic peptide.

Table S5: Echocardiographic analysis of 10-week-old male WT and STZ mice treated with MP, CaP-HA, and CaP-MP.

	Weight (g)	IVSd (mm)	LVIDd (mm)	LVPWd (mm)	IVSs (mm)	LVIDs (mm)	LVPWs (mm)	FS (%)	EF (%)	HR (bpm)	Glycemia (mg/dl)
Basal											
NT	27.2 ± 0.9	0.76 ± 0.03	3.29 ± 0.19	0.78 ± 0.04	1.13 ± 0.06	1.94 ± 0.17	1.21 ± 0.06	41.08 ± 2.50	73.10 ± 3.07	624 ± 38	171 ± 24
MP	26.6 ± 2.0	0.77 ± 0.03	3.31 ± 0.08	0.78 ± 0.03	1.13 ± 0.04	1.97 ± 0.11	1.18 ± 0.06	40.57 ± 2.14	72.51 ± 2.62	585 ± 47	148 ± 26
CaP-HA	27.0 ± 1.7	0.73 ± 0.04	3.33 ± 0.19	0.83 ± 0.04	1.12 ± 0.06	1.96 ± 0.17	1.18 ± 0.04	41.21 ± 1.55	73.26 ± 2.05	620 ± 17	141 ± 31
CaP-MP	27.7 ± 1.6	0.76 ± 0.06	3.25 ± 0.15	0.76 ± 0.04	1.14 ± 0.09	1.91 ± 0.13	1.20 ± 0.04	41.23 ± 1.99	73.34 ± 2.36	590 ± 28	144 ± 31
STZ											
NT	28.4 ± 2.6 ^{***}	0.85 ± 0.05 ^{***}	3.27 ± 0.08	0.81 ± 0.07	1.22 ± 0.05 ^{**}	1.96 ± 0.09	1.21 ± 0.06	40.18 ± 1.64	72.10 ± 2.01	601 ± 28	150 ± 27
MP	27.0 ± 2.0	0.83 ± 0.07 [*]	3.76 ± 0.10 ^{***, \$\$\$}	0.80 ± 0.06	1.12 ± 0.08 ^{\$\$\$}	2.60 ± 0.12 ^{***, \$\$\$}	1.10 ± 0.09 ^{*, \$\$\$}	30.73 ± 2.66 ^{***, \$\$\$}	59.00 ± 3.97 ^{***, \$\$\$}	553 ± 48	417 ± 99 ^{***, \$\$\$}
CaP-HA	26.0 ± 2.0	0.77 ± 0.03 ^{\$\$\$}	3.62 ± 0.20 ^{***, \$\$\$}	0.77 ± 0.03	1.09 ± 0.06 ^{\$\$\$}	2.51 ± 0.18 ^{***, \$\$\$}	1.12 ± 0.04 [§]	30.66 ± 2.30 ^{***, \$\$\$}	59.09 ± 3.41 ^{***, \$\$\$}	552 ± 31	421 ± 28 ^{***, \$\$\$}
CaP-MP	26.2 ± 1.9 ^{***}	0.76 ± 0.03 ^{\$\$\$}	3.66 ± 0.17 ^{***, \$\$\$}	0.75 ± 0.05 [§]	1.03 ± 0.08 ^{*, \$\$\$}	2.59 ± 0.18 ^{***, \$\$\$}	1.06 ± 0.05 ^{***, \$\$\$}	29.19 ± 3.76 ^{***, \$\$\$}	56.82 ± 3.76 ^{***, \$\$\$}	551 ± 32	421 ± 30 ^{***, \$\$\$}
STZ + Treatment											
NT	30.4 ± 1.1	0.78 ± 0.05	3.43 ± 0.19	0.76 ± 0.05	1.16 ± 0.04	2.05 ± 0.15	1.21 ± 0.03	40.31 ± 1.64	72.08 ± 2.03	602 ± 28	178 ± 21
MP	27.2 ± 1.8 ^{§§}	0.80 ± 0.05	3.61 ± 0.12 ^{***}	0.77 ± 0.07	1.13 ± 0.03	2.44 ± 0.14 ^{***, \$\$\$}	1.12 ± 0.09 [†]	32.37 ± 5.18 ^{***, \$\$\$}	61.50 ± 4.06 ^{***, \$\$\$}	607 ± 96	435 ± 124 ^{***, \$\$\$}
CaP-HA	28.9 ± 2.5 ^{\$\$\$}	0.79 ± 0.06	3.64 ± 0.30 ^{***, §}	0.77 ± 0.07 [*]	1.08 ± 0.08 [§]	2.50 ± 0.25 ^{***, \$\$\$}	1.08 ± 0.07 ^{***}	31.51 ± 2.13 ^{***, \$\$\$}	60.28 ± 3.28 ^{***, \$\$\$}	560 ± 45	421 ± 164 ^{***, \$\$\$}
CaP-MP	23.9 ± 3.1 ^{\$\$\$}	0.78 ± 0.03	3.19 ± 0.11 ^{§§}	0.73 ± 0.03	1.10 ± 0.05	1.94 ± 0.06	1.15 ± 0.06	39.18 ± 1.85	70.98 ± 2.38	588 ± 77	466 ± 102 ^{***, \$\$\$}

See Supplementary Table 2 legend for details and description of abbreviations. STZ, streptozotocin (n=10 per each group). * P<0.05, ** P<0.01, *** P<0.005 vs. Basal; § P<0.05 §§ P<0.01, \$\$\$ P<0.001 vs. NT (Two-Way ANOVA).

Table S6: Characterization of LTCC current during rectangular double-pulse protocols and membrane capacities measured in adult cardiomyocytes isolated from treated mice.

	Peak current (pA/pF)	V _{1/2} act (mV)	k act	V _{1/2} inact (mV)	k inact	Reversal potential (mV)	Membrane capacity (pF)
NT	11,01 ± 2,57 ^{***;\$\$\$}	-9,69 ± 4,85	6,28 ± 0,62	-23,72 ± 3,03	4,33 ± 0,54	58,05 ± 7,64	123,5 ± 31,71
MP	6,91 ± 1,57	-10,17 ± 3,70	6,31 ± 1,05	-23,74 ± 3,44	4,27 ± 0,50	56,84 ± 8,39	120,3 ± 23,07
CaP-HA	6,10 ± 1,69	-9,74 ± 4,67	5,98 ± 1,10	-23,56 ± 3,23	4,26 ± 0,57	57,73 ± 6,24	129,1 ± 30,15
CaP-MP	10,49 ± 2,88 ^{***;\$\$\$}	-10,76 ± 3,52	5,90 ± 0,56	-24,64 ± 4,43	4,06 ± 0,42	56,29 ± 5,55	132,5 ± 38,46

V_{1/2} act, potential of half maximal activation; k act, slope factor of activation curve; V_{1/2} inact, potential of half maximal inactivation; k inact, slope factor of inactivation curve (n=16-21 per group). *** P<0.0005 vs. MP; \$\$\$ P<0.0005 vs. CaP-HA (Student's t-test for unpaired samples).

References

1. V. Di Mauro, M. Iafisco, N. Salvarani, M. Vacchiano, P. Carullo, G. B. Ramirez-Rodriguez, T. Patricio, A. Tampieri, M. Miragoli, D. Catalucci, Bioinspired negatively charged calcium phosphate nanocarriers for cardiac delivery of MicroRNAs. *Nanomedicine* **11**, 891-906 (2016).
2. T. Xia, M. Kovoichich, M. Liong, L. Madler, B. Gilbert, H. Shi, J. I. Yeh, J. I. Zink, A. E. Nel, Comparison of the mechanism of toxicity of zinc oxide and cerium oxide nanoparticles based on dissolution and oxidative stress properties. *ACS nano* **2**, 2121-2134 (2008).
3. B. D. Chithrani, A. A. Ghazani, W. C. Chan, Determining the size and shape dependence of gold nanoparticle uptake into mammalian cells. *Nano Lett* **6**, 662-668 (2006).
4. J. Kneipp, H. Kneipp, M. McLaughlin, D. Brown, K. Kneipp, In vivo molecular probing of cellular compartments with gold nanoparticles and nanoaggregates. *Nano Lett* **6**, 2225-2231 (2006).
5. T. Nishikawa, N. Iwakiri, Y. Kaneko, A. Taguchi, K. Fukushima, H. Mori, N. Morone, J. Kadokawa, Nitric oxide release in human aortic endothelial cells mediated by delivery of amphiphilic polysiloxane nanoparticles to caveolae. *Biomacromolecules* **10**, 2074-2085 (2009).
6. P. Nativo, I. A. Prior, M. Brust, Uptake and intracellular fate of surface-modified gold nanoparticles. *ACS nano* **2**, 1639-1644 (2008).
7. L. P. Kozlowski, IPC - Isoelectric Point Calculator. *Biol Direct* **11**, 55 (2016).

8. M. Savi, S. Rossi, L. Bocchi, L. Gennaccaro, F. Cacciani, A. Perotti, D. Amidani, R. Alinovi, M. Goldoni, I. Aliatis, P. P. Lottici, D. Bersani, M. Campanini, S. Pinelli, M. Petyx, C. Frati, A. Gervasi, K. Urbanek, F. Quaini, A. Buschini, D. Stilli, C. Rivetti, E. Macchi, A. Mutti, M. Miragoli, M. Zaniboni, Titanium dioxide nanoparticles promote arrhythmias via a direct interaction with rat cardiac tissue. *Particle and fibre toxicology* **11**, 63 (2014).
9. F. Rusconi, P. Ceriotti, M. Miragoli, P. Carullo, N. Salvarani, M. Rocchetti, E. Di Pasquale, S. Rossi, M. Tessari, S. Caprari, M. Cazade, P. Kunderfranco, J. Chemin, M. L. Bang, F. Polticelli, A. Zaza, G. Faggian, G. Condorelli, D. Catalucci, Peptidomimetic Targeting of Cavbeta2 Overcomes Dysregulation of the L-Type Calcium Channel Density and Recovers Cardiac Function. *Circulation* **134**, 534-546 (2016).
10. A. Alogna, M. Manninger, M. Schwarzl, B. Zirngast, P. Steendijk, J. Verderber, D. Zweiker, H. Maechler, B. M. Pieske, H. Post, Inotropic Effects of Experimental Hyperthermia and Hypothermia on Left Ventricular Function in Pigs-Comparison With Dobutamine. *Critical care medicine* **44**, e158-167 (2016).